Intelligent Fault Detection Algorithm Based on H_i/H_∞ Optimization and a Cascaded Neural Networks

Muzhuang Guo[1], Chen Guo[2], Chuang Zhang[1], Xinyu Zhang[1]* and Yuanchang Liu[3]*

[1]Navigation College, Dalian Maritime University, Dalian, China
[2]Marine Engineering College, Dalian Maritime University, Dalian, China
[3]Department of Mechanical Engineering, University College London, London, UK

(* Corresponding authors: Yuanchang Liu, yuanchang.liu@ucl.ac.uk; Xinyu Zhang, zhangxy@dlmu.edu.cn)

Abstract
Autonomous surface ships (ASSs) have attracted attention owing to their ability to perform various tasks in complex and challenging aquatic environments without relying on a crew. However, they require reliable sensors to ensure navigational safety. In this study, a robust and intelligent fault detection algorithm was designed for the integrated navigation system of an ASS. First, a residual observer-based fault detection algorithm using H_i/H_∞ optimization is proposed to deal with process disturbances and measurement noise. Such noise can be modeled under the condition of a bounded l_2-norm to account for the sensitivity and robustness of the residual observer against random noise with unknown properties. However, this fault detection algorithm is insensitive to soft faults, which manifest as noise characterized by a small amplitude and slow variation. Conventional strategies for evaluating the fault detection threshold rely on human experience, which is insufficiently sophisticated for fault detection. Therefore, a cascaded neural network is proposed for optimizing the fault detection algorithm when the amount of training data is limited. The cascaded neural network consists of a multi-feature time domain network, a frequency-domain fault detection network as well as a decision-level fusion network. The proposed algorithm was verified in simulations as well as on historical data collected from real ship sensors. The results demonstrated that the proposed algorithm offers intelligent fault detection, including soft faults, with a low false alarm rate for integrated navigation systems.

Key words: integrated navigation system, robust fault detection, H_i/H_∞ optimization, cascaded neural network

1. Introduction
According to Fan et al. (2020), an autonomous surface ship (ASS) can function independently of human input to varying degrees. An ASS comprises three primary systems: control, navigation, and propulsion. The navigation system feeds information on the motion state to the control system, which is critical for ensuring safe and reliable navigation. The integrated navigation system of an ASS includes the ship's inertial navigation system (SINS), a global navigation satellite system (GNSS), such as the Global Positioning System (GPS), the Doppler velocity log (DVL), and the navigation radar, each of which offers advantages and disadvantages. At present, improving the performance of a single navigation technology is inconvenient. A more common approach is to combine the information from multiple sensors to improve navigational accuracy. However, previous studies (Liu et al. 2016; Thombre et al. 2022) have shown that introducing additional sensors to increase the estimation robustness and accuracy of the integrated navigation system also considerably increases its complexity. If a fault occurs in the subsystems of the integrated navigation system, this could generate catastrophic effects through feedback control (Chen et al. 2020). Considering the complex operating environments of ASSs, robust state estimation algorithms have been proposed to account for unknown input noise. Accurately detecting sensor failures in the presence of uncertain inputs is an important research subject (Wang et al. 2022) with some studies already applied fault detection technology to ASS communication systems (Thombre et al. 2022). Consequently, this field has attracted considerable research attention and many fault detection methods have been proposed, which can be broadly classified as model-based or model-free (Gao et al. 2015; Gao, Cecati, & Ding 2015).

Model-based fault detection methods can be further divided into those based on a residual observer (Miao et al. 2014) and those based on a state observer (Yu et al. 2021). These methods use a Kalman filter to create state or information residual statistics and determine if an integrated navigation system has a fault based on the probability distribution it follows. However, this algorithm is highly dependent on the system and measurement noises satisfying the constraint of noncorrelated zero-mean white Gaussian noise (Li et al. 2020), and it cannot guarantee that the evaluation function of the observer is robust against uncertain noise and sensitive to faults. To solve this limitation, several researchers (Chen et al. 2000; Liu et al. 2018; Khan et al. 2014) have applied H_i/H_∞ optimization to discrete-time nonlinear systems. Zhong et al. (2016) proposed a fault detection algorithm for optimizing the SINS/GNSS integrated navigation system in the presence of normally distributed disturbances. Liu et al. (2019) proposed a new residual evaluation function for the H_i/H_∞ optimization of discrete-time nonlinear systems. However, this residual observer-based extended H_i/H_∞ algorithm is restricted by the linearization accuracy of the dynamic model for Taylor expansion in the extended Kalman filter framework, which could result in a large state estimation error and high false alarm rate. Residual observer-based methods are often limited by their dependence on known model parameters, and the detection threshold is difficult to define, so they are often not sensitive enough to detect soft faults, which are characterized by a slow change or small amplitude (Sun et al. 2021).

To address this limitation, data-driven fault detection algorithms have been extensively studied (Gao, Cecati & Ding et al. 2015). Xi et al. (2018) showed that the fundamental principles of fault detection algorithm based on signal processing include the following steps: (1) extracting the time or frequency domain features from the output information of the system under various operating conditions, and (2) using the extracted statistical eigenvalues for fault detection. Zhu et al. (2016) proposed a fault detection function that comprises the predicted and actual innovations of the Kalman filter in addition to their variance. Zhong et al. (2017) proposed a soft fault detection method that incorporates the least-squares support vector machine (LS-SVM) regression theory into the autonomous integrity monitored extrapolation framework. Yang et al. (2020) proposed a fault detection algorithm based on the similarities between support vector machine (SVM) and principal component analysis. Zanoli et al. (2012) proposed a method for the real-time detection of soft and hard faults in an integrated navigation system. Several researchers have considered combining data-driven fault detection with a neural network. Guo et al. (2018) proposed a convolutional neural network (CNN)-based algorithm for detecting frequency-domain signal faults in unmanned aerial vehicle sensors. However, extracting features from the original sensor signal depends on the data volume, and different models are needed for different sensors. Thus, such methods lack generality and are difficult to be applied to the integrated navigation systems of ASSs operating in a complex environment.

It can be summarized that the current research on fault detection of integrated navigation systems has the following deficiencies. First, model-based fault detection is not sufficiently robust against unknown system noises and statistical characteristics. Second, residual observer-based fault detection normally relies on human experience to determine the threshold settings and is not sensitive to soft faults. Finally, many researchers have proposed using deep learning to solve the above problems, but most built a neural network for a single sensor, and training such networks requires a large amount of data. Extracting a large number of fault samples from the integrated navigation systems of an ASS is unrealistic.

Thus, accurate fault detection for the integrated navigation system of an ASS that does not rely on model constraints, or a large amount of data is an important research challenge. In this study, a new fault detection algorithm was developed using H_i/H_∞ optimization and multiple neural networks to have an improved sensitivity to faults and robustness against unknown inputs. The main contributions of the proposed algorithm are as follows:

1. The algorithm was designed according to the cubature Kalman filter (CKF) framework so that it is theoretically unaffected by linearization of kinetic model in contrast to the extended H_i/H_∞ fault detection algorithm.

2. The optimization by a cascaded neural network does not rely on empirical parameters such as the threshold of the evaluation function making the proposed detection algorithm have an improved sensitivity to soft faults.

3. The proposed algorithm was verified through extensive simulations as well as real ship data. The fault detection process functions perform well in all cases where limited sample data are available.

The rest of the paper is organized as follows. Section 2 introduces the commonly used error state and measurement equations for the integrated navigation systems of an ASS. Section 3 presents the proposed fault detection algorithm and the optimization using a cascaded neural network. Section 4 presents the verification of the algorithm through simulations and historical ship data. Section 5 concludes the paper.

2. Integrated navigation system and its error model

The most commonly used sensors to measure the motion state of an ASS are SINS, GNSS, DVL, and the BeiDou Navigation Satellite System (COMPASS). The error models associated with these sensors have significant impact on the accuracy and performance of the entire integrated navigation system.

2.1 Error state equation

MEMS-SINS comprises three microelectromechanical system (MEMS) gyroscopes and three accelerometers. The navigation coordinate system (*n*-frame) is defined according to the east–north–up system. The origin of the body frame (*b*-frame) is located at the centroid of the vessel. The Earth-centered Earth-fixed frame (ECEF, *e*-frame) and the inertial frame (ECI, *i*-frame) originate at the center of Earth. However, the *i*-frame does not rotate in lockstep with the fixed stars. Figure 1 shows the relationships between different frames.

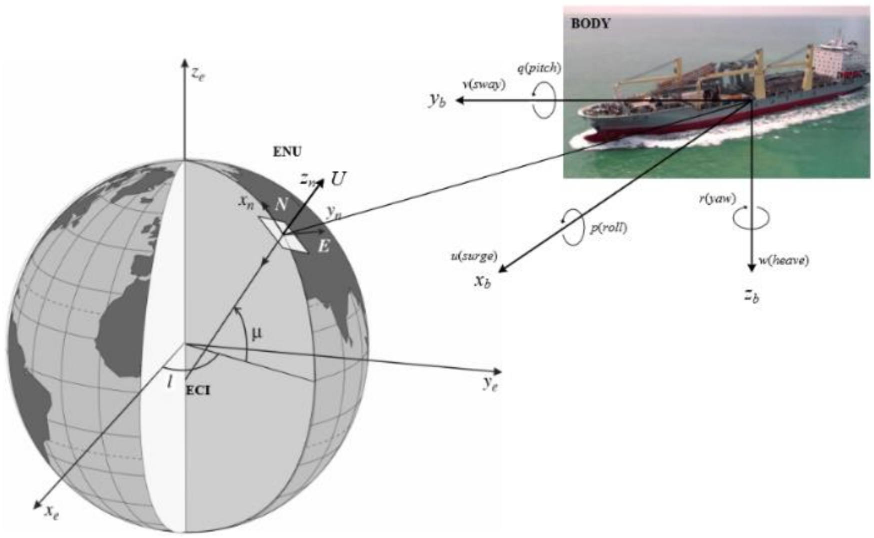

Figure 1. Reference frames and notation of variables for a vessel.

The nonlinear SINS error model can be expressed as follows:

$$\begin{cases} \dot{\phi}^n = \phi^n \times \omega_{in}^n + \delta\omega_{in}^n - C_b^n \omega_{ib}^b - \varepsilon^n \\ \delta\dot{V}^n = -\phi^n \times f^n + C_b^n f^b + \delta V^n \times (2\omega_{ie}^n + \omega_{en}^e) \\ \qquad + V^n \times (2\delta\omega_{ie}^n + \delta\omega_{en}^e) + \nabla^n \\ \delta\dot{P}^n = \delta V^n + \rho \times \delta P^n \end{cases} \tag{1}$$

where ϕ^n, δV^n, and δP^n are the attitude, velocity, and position error vectors, respectively, in the *n*-

frame. ε^n and ∇^n are the vectors of the gyroscope and accelerometer noises, respectively. ω_{ab}^c $(a,b,c=i,e,n)$ is the local Earth rotation rate in the b-frame with respect to the a-frame expressed in the c-frame (Wang et al. 2017). $\rho=[-\dot{L},\ \dot{\lambda}\cos L,\ -\dot{\lambda}\sin L]^{\mathrm{T}}$, where L, λ, and h are the latitude, longitude, and height, respectively. C_b^n is the attitude transformation matrix between the b-frame and n-frame (Wei et al. 2018). Thus, the continuous-time nonlinear state equation for an integrated navigation system can be expressed as follows:

$$\dot{x}_t = f_c(x_t) + B_c\omega_t \tag{2}$$

where $x_t=[\delta P^n, \delta V^n, \phi^n, \varepsilon^n, \nabla^n]$ and $\omega_t=[\varepsilon^n,\ \nabla^n]$. f_c and B_c denote the nonlinear coupling system equations for transferring the state variables x_t and unknown noise ω_t in Equation (1).

2.2 Measurement equations

The following discrete-time equation is usually used to express the measurement function:

$$z_t = H_t x_t + v_t \tag{3}$$

where z_t is the measurement vector, H_t is the observation matrix, and v_t is the vector of the measurement noise. SINS can be used as the reference navigation system to ensure high precision. Thus, SINS/GNSS and SINS/DVL/COMPASS integrated navigation systems are often adopted to realize autonomy and accuracy.

For the SINS/GNSS integrated navigation system, the measurement vector z_t^{sg} comprises the difference between the position and velocity obtained using SINS and GNSS (Shen et al. 2019). v_t^{sg} is the measurement noise of the SINS/GNSS integrated navigation system:

$$z_t^{sg} = \begin{bmatrix} L_t^{SINS} - L_t^{GNSS} \\ \lambda_t^{SINS} - \lambda_t^{GNSS} \\ h_t^{SINS} - h_t^{GNSS} \\ V_{E,t}^{SINS} - V_{E,t}^{GNSS} \\ V_{N,t}^{SINS} - V_{N,t}^{GNSS} \\ V_{H,t}^{SINS} - V_{H,t}^{GNSS} \end{bmatrix} \tag{4}$$

The measurement equation for the SINS/GNSS integrated navigation system is as follows:

$$z_t^{sg} = \begin{bmatrix} I_{3*3} & 0_{3*3} & 0_{3*9} \\ 0_{3*3} & I_{3*3} & 0_{3*9} \end{bmatrix} x_t + v_t^{sg} \tag{5}$$

For the SINS/DVL/COMPASS integrated navigation system, the measurement information comprises the difference between the east–north velocities and headings obtained using SINS, DVL, and COMPASS:

$$z_t^{sdc} = \begin{bmatrix} V_{E,t}^{SINS} - V_{E,t}^{DVL} \\ V_{N,t}^{SINS} - V_{N,t}^{DVL} \\ \psi_t^{SINS} - \psi_t^{COMPASS} \end{bmatrix} \tag{6}$$

Thus, the measurement equation for the SINS/DVL/COMPASS integrated navigation system is as follows:

$$z_t^{sdc} = \begin{bmatrix} 0_{1*2} & 1 & 0_{1*3} & 0_{1*3} & 0_{1*3} \\ 0_{3*2} & 0_{3*1} & I_{3*3} & 0_{3*3} & 0_{3*3} \end{bmatrix} x_t + v_t^{sdc} \quad (7)$$

v_t^{sdc} is the measurement noise of the SINS/DVL/COMPASS integrated navigation system.

2.3 Integrated navigation system based on the cubature Kalman filter

For an integrated navigation system comprising the error state system of Equation (2) and measurement system of Equation (3), Fig. 2 shows the estimation error of the motion state and process of correcting the SINS output. The system noise is $\omega_k \sim N(0, Q_k)$, and the random measurement noise is $v_k \sim N(0, R_k)$. Therefore, a Gaussian filter with a Kalman filter structure can be used to process the nonlinear discrete integrated system at step k in the state estimation task while the time and measurement are being updated. The details of the CKF algorithm for the integrated navigation system is given in Appendix I.

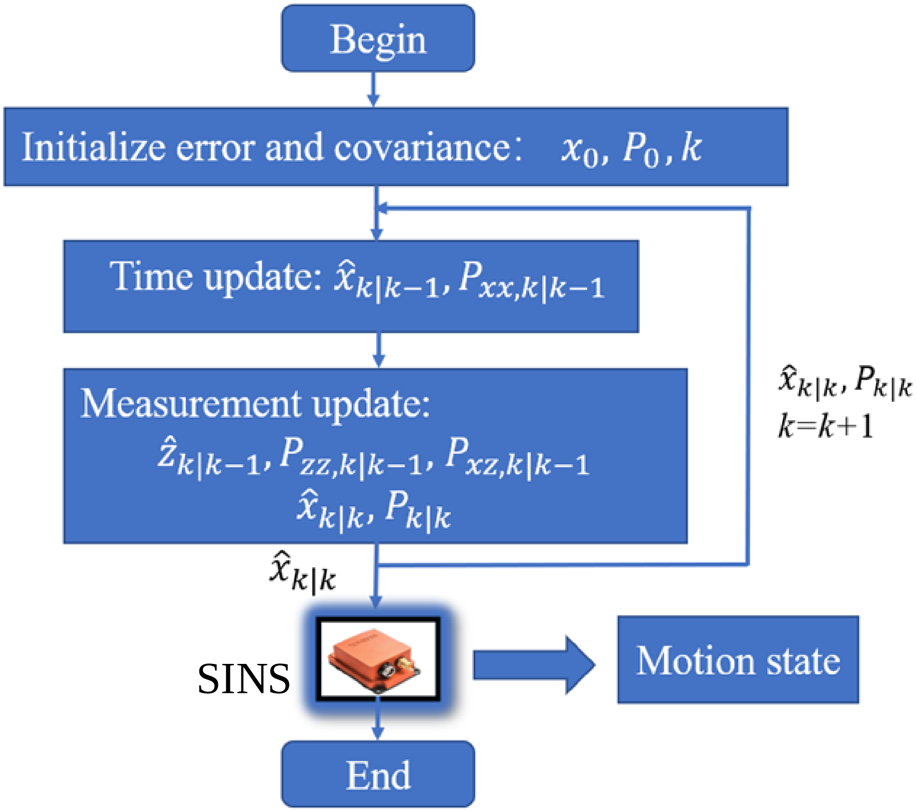

Figure 2. CKF-based integrated navigation system.

When an ASS is cruising at sea, ω_k and v_k are affected by the complex environment, such as thermal changes and electromagnetic interference. The properties of random errors may be uncertain and variable, which contradicts the requirement of the Kalman filter for zero-mean Gaussian white noise. This random error will lead to significant measurement error or even failure of the angular velocity and acceleration, which will affect one-step state prediction ($\hat{x}_{k|k-1}$) and prediction variance ($P_{xx,k|k-1}$) in the time update. Furthermore, GNSS and DVL frequently encounter measurement outliers, which will lead to errors in measurement matrix (z_k) at k step and affect the filter gain. This in turn reduces the state estimation accuracy. The above faults eventually affect state prediction covariance matrix ($P_{k|k}$) and will contaminate the output of the integrated navigation system in step $k+1$.

3. Proposed fault detection algorithm

In addition to accurate motion state estimation, the increased demand for reliability has increased the importance of fault detection for the integrated navigation system of an ASS. Therefore a new fault detection algorithm has been proposed with the details described below.

3.1 Residual observer-based fault detection using CKF and H_i/H_∞ optimization

To account for the sensitivity to faults and robustness against unknown random noise of the residual observer, a fault detection algorithm is proposed for a time-varying nonlinear integrated navigation system using H_i/H_∞ optimization. Much of the theory behind the proposed algorithm is based on the research of Zhong et al. (2015). The fault case for a nonlinear state-space model of integrated navigation system can be expressed as

$$\begin{cases} \dot{x}_t = f_c(x_t) + B_c\omega_t + B_{cf,t} f_{1,t} \\ z_t = H_t x_t + v_t + D_{cf,t} f_{2,t} \end{cases} \tag{8}$$

where $f_{1,t}$ and $f_{2,t}$ are the SINS and measurement faults, respectively. Unlike Zhong et al. (2015, 2016), the proposed algorithm adopts CKF to satisfy the accuracy and robustness requirements for motion state estimation of a strongly nonlinear integrated navigation system. The first step of designing a residual observer-based fault detection filter is the discrete linearization of f_c as:

$$\begin{aligned} & f_c(x_t)=A_k x_k + \xi_k \\ & \{\hat{A}_k\} = \arg\min \frac{1}{2n}\sum_{k=1}^{2n} \xi_k^T \xi_k \end{aligned} \tag{9}$$

where $\xi_k = \gamma_k - A_k\chi_k$ and γ_k are the $2n$ sampling result of a one-step state prediction. Then, $A_k = (\chi_k\chi_k^{\mathrm{T}})^{-1}(\chi_k\gamma_k^{\mathrm{T}})$ can be obtained using culture point sampling. A_k is the result from the linearization of f_c. d_k and f_k are assumed to be $l_2[0,N]$-norm bounded uncertain disturbances and measurement noise in step k.

Thus, the nonlinear discrete-time dynamic system of Equation (8) can be rewritten as follows:

$$\begin{cases} x_{k+1} = A_k x_k + B_c d_k + B_f f_k + \xi_k \\ z_{k+1} = H_k x_k + D_c d_k + D_f f_k \end{cases} \tag{10}$$

where $f_k = [f_{1,t}^{\mathrm{T}}, f_{2,t}^{\mathrm{T}}]^{\mathrm{T}}$, $B_f = [B_{cf,t}, 0]$, and $D_f = [0, D_{cf,t}]$. The following observer-based fault detection function is then used to generate residuals:

$$\begin{cases} \hat{x}_{k+1} = A_k\hat{x}_k + K_k\tilde{y}_k + \xi_t \\ \tilde{y}_k = z_k - H_k\hat{x}_k \\ r_k = W_k\tilde{y}_k \end{cases} \tag{11}$$

where r_k is the residual, K_k is the gain matrix, and W_k is the postfilter. Note that $\hat{x}_k$ is the state estimation. If $A_{dk} = A_k - K_k H_k$, $B_{dk} = B_c - K_k D_c$, $B_{fk} = B_f - K_k D_f$, and $D_{dk} = D_c$, then the state estimation error $\tilde{x}_k = x_k - \hat{x}_k$ can be obtained as follows:

$$\begin{cases} \tilde{x}_{k+1} = A_{dk}\tilde{x}_k + B_{dk}d_k + B_f f_k \\ \tilde{y}_k = H_k\tilde{x}_k + D_{dk}d_k + D_f f_k \\ r_k = W_k\tilde{y}_k \end{cases} \tag{12}$$

The following is defined:

$$
\begin{aligned}
&\left\|G_{rd}\right\|_{\infty[0,N]}^{2}=\sup_{f_t=0}\frac{\sum_{k=0}^{N}\left\|r_k\right\|_2^2}{\sum_{k=0}^{N}\left\|d_k\right\|_2^2+\left\|\tilde{x}_0\right\|_2^2}\\
&\left\|G_{rf}\right\|_{\infty[0,N]}^{2}=\sup_{\tilde{x}_0=0,d_k=0}\frac{\sum_{k=0}^{N}\left\|r_k\right\|_2^2}{\sum_{k=0}^{N}\left\|f_k\right\|_2^2}\\
&\left\|G_{rf}\right\|_{-[0,N]}^{2}=\inf_{\tilde{x}_0=0,d_k=0}\frac{\sum_{k=0}^{N}\left\|r_k\right\|_2^2}{\sum_{k=0}^{N}\left\|f_k\right\|_2^2}
\end{aligned}
\tag{13}
$$

where $\left\|G_{rd}\right\|_{\infty[0,N]}^{2}$ is the robustness to unknown inputs and $\left\|G_{rf}\right\|_{\infty[0,N]}^{2}$, $\left\|G_{rf}\right\|_{-[0,N]}^{2}$ are the best and worst-case sensitivities, respectively, of the residual to faults.

If $\phi_{k,j}=A_{dk}A_{dk-1}...A_{dj}$, $\phi_{j,j}=I$ as per Zhong et al. (2010), then Equation (12) can be rewritten as follows:

$$
r_N=\Gamma_0\tilde{x}_0+\Gamma_d d_N+\Gamma_f f_N \tag{14}
$$

where

$$
\Gamma_0=\begin{bmatrix} W_0H_0\\ W_1H_1\phi_{1,0}\\ \vdots\\ W_NH_N\phi_{N,0}\end{bmatrix}
$$

$$
\Gamma_d=\left[\Gamma_{d(k,j)}\right]_{(N+1)*(N+1)}
$$

If $k<j$, then $\Gamma_{d(k,k)}=W_kD_{dk}$ and $\Gamma_{d(k,j)}=0$. If $k>j$, then $\Gamma_{d(k,j)}=W_kH_k\phi_{k-1,j}B_{jd}$. Similarly, Γ_f can be used to replace D_f and B_f in Equation (12). Then, Equation (13) can be rewritten as follows:

$$
\max\frac{\left\|G_{rf}\right\|_{\infty,[0,N]}}{\left\|G_{rd}\right\|_{\infty,[0,N]}},\max\frac{\left\|G_{rf}\right\|_{-,[0,N]}}{\left\|G_{rd}\right\|_{\infty,[0,N]}} \tag{15}
$$

To satisfy Equation (15), both postfilter (W_k) and gain (K_k) can be approximated as follows:

$$
\begin{cases}
K_k=(A_kP_kH_k^{\mathrm{T}}+B_cD_c^{\mathrm{T}})R_{\tilde{y}k}^{-1}\\
R_{\tilde{y}k}=H_kP_kH_k^{\mathrm{T}}+D_cD_c^{\mathrm{T}}\\
P_{k+1}=A_kP_kA_k^{\mathrm{T}}+B_cB_c^{\mathrm{T}}-K_kR_{\tilde{y}k}K_k^{-1}\\
W_k=R_{\tilde{y}k}^{-1}
\end{cases}
\tag{16}
$$

The following equation is commonly used to evaluate residual observer-based fault detection filters:

$$
J_N=1/N\sum_{k-N}^{k}r_kr_k^{\mathrm{T}} \tag{17}
$$

where N is the sliding window width. A fault alarm is triggered when J_N exceeds a predefined threshold. Algorithm 1 summarizes the proposed fault detection algorithm based on CKF and H_i/H_∞ optimization for an integrated navigation system subject to energy-bounded random errors and measurement noises.

Algorithm 1 Proposed fault detection algorithm

Step 1:	Set step $k=0$, $\hat{x}_0 = 0_{1*15}$;
Step 2:	Obtain the linearized system matrix A_k and ξ_k with (9);
Step 3:	Calculate L_k and W_k using (16);
Step 4:	Calculate $\hat{x}_{k+1}$ and r_{k+1} using (11);
Step 5:	Calculate J_N with (17);
Step 6:	Choose a threshold and comparing with (17) to detect faults;
Output:	Boolean value of whether the fault exists

3.2 Optimization of the fault detection algorithm using a cascaded neural network

The proposed algorithm offers the advantages of sensitivity to faults and robustness against unknown inputs. Consequently, it can obtain reliable fault detection results. However, it is based on a residual observer, which is insensitive to soft faults. This affects the one-step state prediction of the Kalman filter and makes the state estimation track the fault values. Thus, the residual error changes are not evident. Moreover, the limitations of the sliding window width and the difficulty in determining the J_N threshold in Equation (17) need to be considered. Thus, Fig. 3 shows a framework of using a cascaded neural network to optimize the proposed fault detection algorithm.

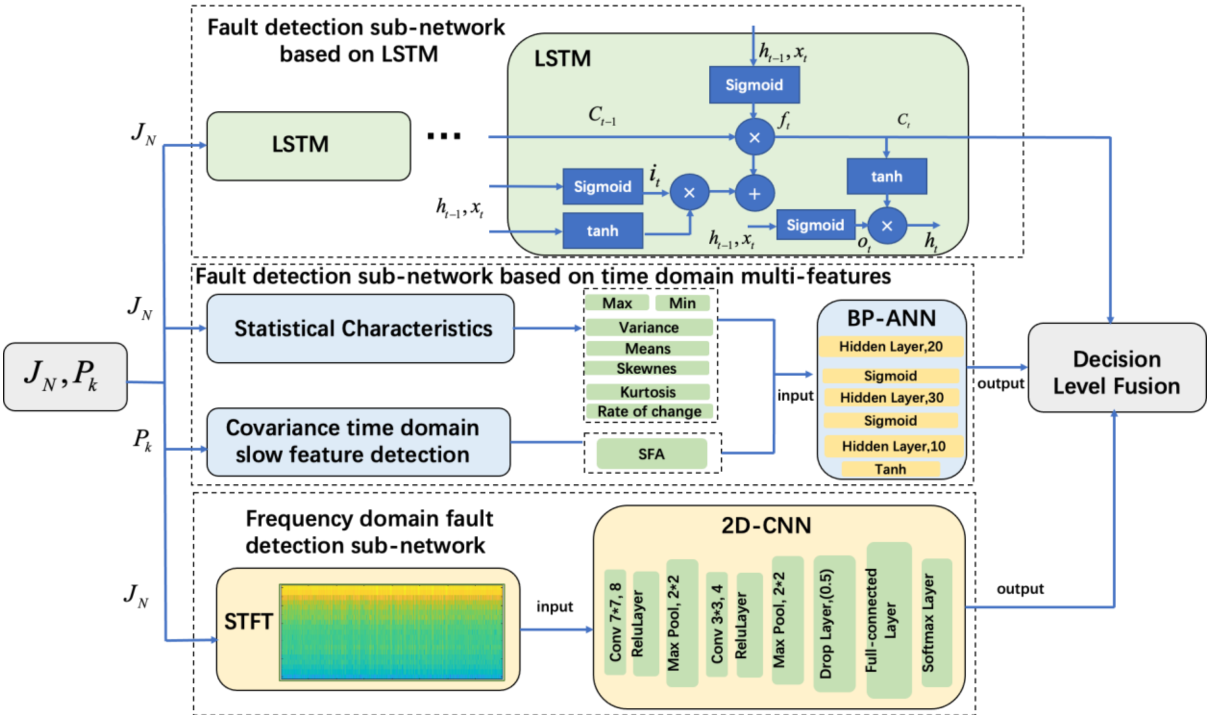

Figure 3. Framework for optimizing the proposed fault detection algorithm using a cascaded neural network.

Table 1. Features extracted from the residual J_N signal

Features	Description
Mean	$\mu = 1/N\sum_{n}^{n+N} x_n$
Max	$\mathrm{Max}(x_n)$
Min	$\mathrm{Min}(x_n)$
Variance	$\sigma^2 = 1/N\sum_{n}^{n+N}(x_n-\mu)^2$
Skewness	$1/N\sigma^3\sum_{n}^{n+N}(x_n-\mu)^3$
Rate of change	$\max(\sum_{n}^{n+N}(x_{n+1}-x_n))$
kurtosis	$1/N\sigma^4\sum_{n}^{n+N}(x_n-\mu)^4$

To address this limitation, time-domain features can be extracted for the state estimation error covariance P_k, which is more severely affected by faults in the state estimation of the integrated navigation system. This is particularly helpful for the attitude, which has weak observability. Slow feature analysis (SFA) was used to extract the time-domain features of the covariance P_k owing to its ability to extract slowly changing fault signal features in a high-dimensional input. The following set of equations $f_j()$ is used to identify slowly varying components $y_j(k)$ from P_k:

$$y_j(k) = f_j(P_k) \tag{18}$$

where $f_j(P_k) = [f_1(P_k), f_2(P_k), ..., f_m(P_k)]$ is a set of proper functions. The primary objective function of SFA is given by

$$\min \Delta y_j(k) = \min \left\langle \dot{y}_j^2(k) \right\rangle \tag{19}$$

under the constraints of

$$\begin{aligned} &\left\langle y_j(k) \right\rangle = 0 && \text{(zero mean)} \\ &\left\langle y_j^2(k) \right\rangle = 1 && \text{(unit variance)} \\ &\forall i < j, \left\langle y_j(k) y_j(k) \right\rangle = 0 && \text{(decorrelation)} \end{aligned} \tag{20}$$

where $\dot{y}_j(k)$ is the first derivative of $y_j(k)$ at transient step k and $\langle . \rangle$ is the mean value of the signal. However, obtaining the nonlinear mapping $f_j()$ directly is difficult. To address this limitation, a kernel transformation $S_{ij} = s(P_k(i), P_k(j))$ is used on the inputs P_k to determine the kernel characteristics, where $i, j = 1.....n$ denote the n th-dimensional input signals (Du et al. 2019). The kernel transformation vector can be determined as follows:

$$m\lambda\alpha = \tilde{S}\alpha \tag{21}$$

The slowest- and second-slowest features correspond to the smallest and second-smallest values, respectively, of λ. m is the number of samples, and the new principal component features of the kernel can be acquired by

$$v'_{kj} = \sum_{i=1}^{d} \alpha_i^j \tilde{S}(P_k, P_k(i)) \tag{22}$$

where v'_k is zero-mean uncorrelated vector. To satisfy the constraints of Equation (20), an additional transformation should be applied to v'_k that does not change the mean, variance:

$$y_k = G^T v'_k \tag{23}$$

The objective of Equation (19) can be realized by transforming it into a problem of solving eigenvalues to obtain G (Zhang et al. 2021). Then, the optimal solution is given by $G^T = [g_{,0}, g_{,1}, ..., g_{d-1}]$, where the order of eigenvalues is from small to big.

In addition to the time-domain fault features extracted from LSTM and prior knowledge, the frequency-domain characteristics of the original signal are important for determining the signal quality. Thus, a sub-CNN network was adopted for frequency-domain fault detection based on short-time Fourier transform (STFT). The mathematical expression of the STFT is as follows:

$$ST(\omega,\tau) = \int f(t) g^*(t-\tau) e^{-j\omega t} dt \tag{24}$$

where * is a conjugate symbol and $g(t)$ is the Hamming window function (Tao et al. 2019). To avoid the influence of extreme values on the learning efficiency of the neural network, the wavelet transform is used to extract the envelope of the signal change trend before the frequency-domain feature extraction. Because the noise of an integrated navigation system is relatively stable under normal operating conditions, the quality of the integrated navigation system can be measured using the fundamental and harmonic waves of J_N. The content of the fundamental wave can accurately reflect the noise distribution of SINS and external measurement sensors, i.e., ideal periodic noise. The harmonic wave reflects the fault and additional noise based on an ideal periodic signal because the solution period of an integrated navigation system is a fixed and nonstationary signal. Then, multidimensional frequency-domain characteristics extracted by STFT are substituted into the CNN for training (Guo et al. 2018). Finally, the training results of the LSTM-based fault detection subnetwork, multi-feature time-domain fault detection subnetwork, and frequency-domain fault detection subnetwork are used as inputs to the backpropagation (BP)-based decision-level fusion network to achieve online fault detection.

As shown in Fig. 3, the normalized J_N is substituted into the LSTM-based fault detection subnetwork comprising ten LSTM neuron units as training data. The BP-ANN in the multi feature time-domain fault detection subnetwork has a structure of 30 hidden layers and 10 output layers. The 2D-CNN in the frequency-domain fault detection subnetwork has the following structure: one input layer connected to eight 7 × 7 convolutional layers, a 2 × 2 max pooling layer, four 3 × 3 convolutional layers, another 2 × 2 maximum pooling layer, and final output to two full connection layers. The detection results of the three networks are integrated in the decision-level fusion network.

4. Verification

4.1 Simulation

Simulations were performed using the XSENS Mti-710 inertial measurement unit (IMU). The gyroscope and accelerometer have in-run bias stabilities of 10°/h and 15 µg, respectively, and noise densities of 0.01°/s/sqrt (Hz) and 60 µg/sqrt (Hz), respectively. As the external measurement unit, the GNSS of the integrated navigation system had a positioning error of 5 m and velocity error of 0.4 m/s. The simulation error data of Mti-g-710 were taken from the instruction manual, and the simulation errors of GNSS and DVL were within reasonable ranges (Jin et al. 2022).

The propeller of the ASS was assumed to rotate at a constant speed in the face of a 3 m/s west wind and 1 m/s crosscurrent with an initial speed of 15.5 knots and heading of 000°. The heading was fine-tuned during 0–800 s. Then, the rudder angle was adjusted to 10° and −10° at 1000–1400 s and 1400–2000 s, respectively, and to 25° and −25° at 2000–2500 s and 2500–3000 s, respectively. Figure 4 shows the simulated motion trajectory.

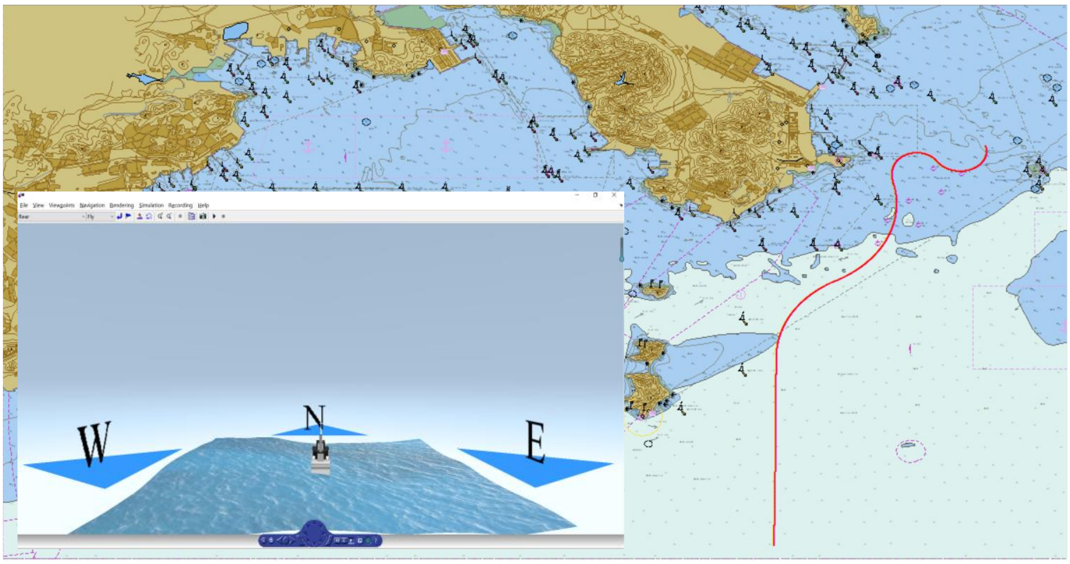

Figure 4. Diagram of the ship motion trajectory and simulation system interface.

Various simulation cases were input with different J_N and P_k under normal and fault conditions. The different subnetworks were pretrained 10,000 times, and the decision-level fusion network was trained 22,000 times. The batch size was set to 50 based on the loss values and accuracy from the cross-experiments. The learning rate was set to be 0.0001. The training goal (i.e., minimum mean square error, MMSE) was set as 10^{-4} for all subnetworks except the multi-feature time-domain fault detection subnetwork. This subnetwork was set to a learning rate of 0.001 and an MMSE of 10^{-6}. For the frequency-domain fault detection subnetwork, the packet loss rate was set as 0.5 to avoid overfitting. For the decision-level fusion network, the training rate and MMSE were set the same as for the multi-feature time-domain fault detection subnetwork.

The training results are shown in Fig. 5. For the LSTM-based fault detection subnetwork [Fig. 5(a)] and CNN-based frequency-domain fault detection subnetwork [Fig. 5(c)], the error of the loss function gradually converged and the classification accuracy gradually improved, which indicates that the network performances tended to be stable. For the multi-feature time-domain fault detection subnetwork [Fig. 5(b)] and BP-based decision-level fusion network [Fig. 5(d)], the gradient and RMSE gradually decreased, which indicates that the trained networks tended to be stable. After all iterations, the three subnetworks had accuracy rates of 90.21%, 95.24%, and 99.32%, and the decision-level fusion network had an accuracy rate of 99.6%.

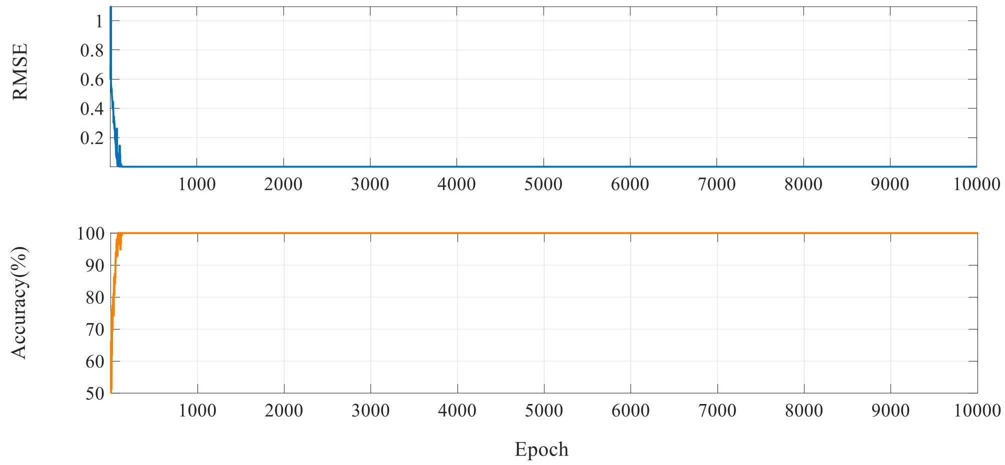

(a) LSTM-based fault detection subnetwork.

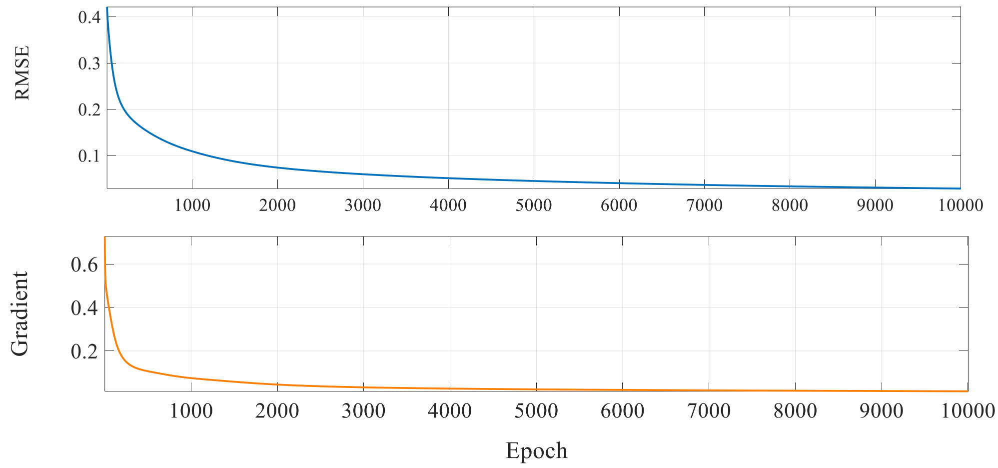

(b) Multi-feature time-domain fault detection subnetwork.

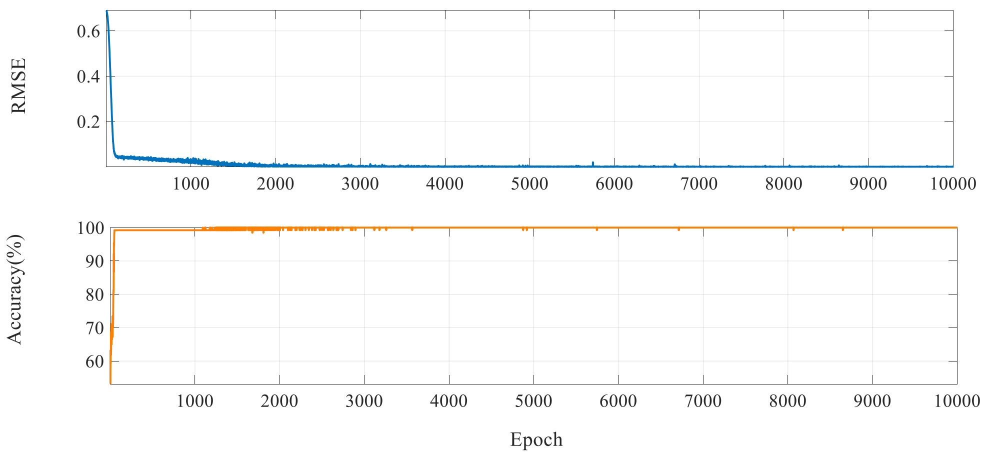

(c) Frequency-domain fault detection subnetwork.

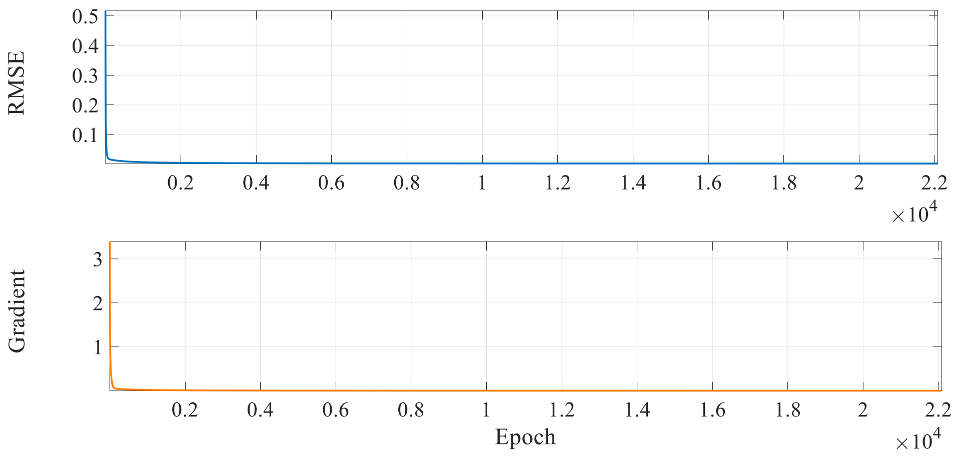

(d) Decision-level fusion network.

Figure 5. Training results of the subnetworks.

Various faults that may occur in ship sensors were simulated to confirm the effectiveness of the proposed algorithm. The SINS/GNSS integrated navigation system was considered as a research object to verify the effectiveness of the SINS/DVL/COMPASS integrated navigation system. External measurement faults primarily manifest as signal interruptions caused by interference or shielding as well as hard faults with increased errors in a short time period. Temperature, violent motion, and electromagnetic interference all affect the IMU primarily through soft faults that cause errors to accumulate over time. Table 2 summarizes the simulated hard and soft faults added to the SINS/GNSS integrated navigation system, where δP_{GNSS} and δV_{GNSS} are the position and velocity errors of GNSS, and ε_k is the gyroscope error of the IMU. It is worth noting that the faults simulated in this paper mainly include the hard faults, which can be denoted as a step-function type commonly seen in GNSS and DVL output data. The additive noise failure caused by noise drift and the additive Gaussian measurement noise can be regarded as soft failure, which comes with increasing error variance and often occur in SINS and GNSS.

Table 2. Simulated hard and soft faults added to the SINS/GNSS integrated navigation system

<table>
<tr><th></th><th>Time</th><th>Faults</th><th>Types</th></tr>
<tr><td>1</td><td>110 s < t < 120 s
1110 s < t< 1120 s
2110 s < t< 2120 s</td><td>$\delta P_{GNSS} = 1.5 * \delta P_{GNSS}$
$\delta P_{GNSS} = 2 * \delta P_{GNSS}$</td><td rowspan="3">Soft faults</td></tr>
<tr><td>2</td><td>210 s < t < 220 s
1210 s < t< 1220 s
2210 s < t < 2220 s</td><td>$\delta V_{GNSS} = 1.5 * \delta V_{GNSS}$
$\delta V_{GNSS} = 2 * \delta V_{GNSS}$</td></tr>
<tr><td>3</td><td>310 s < t < 320 s
1310 s < t < 1320 s
2310 s < t < 2320 s</td><td>$\delta V_{GNSS} = 1.5 * \delta V_{GNSS}$
$\delta P_{GNSS} = 1.5 * \delta P_{GNSS}$
$\delta V_{GNSS} = 2 * \delta V_{GNSS}$
$\delta P_{GNSS} = 2 * \delta P_{GNSS}$</td></tr>
<tr><td>4</td><td>410 s < t < 420 s
1410 s < t < 1420 s
2410 s < t < 2420 s</td><td>$\delta V_{GNSS} = \delta V_{GNSS} + 1$ (m/s)
$\delta V_{GNSS} = \delta V_{GNSS} + 2$(m/s)</td><td rowspan="3">Hard faults</td></tr>
<tr><td>5</td><td>510 s < t < 520 s
1510 s < t < 1520 s
2510 s < t < 2520 s</td><td>$\delta P_{GNSS} = \delta P_{GNSS} + 3$(m)
$\delta P_{GNSS} = \delta P_{GNSS} + 6$ (m)</td></tr>
<tr><td>6</td><td>610 s < t < 620 s
1610 s < t < 1620 s
2610 s < t < 2620 s</td><td>$\delta P_{GNSS} = \delta P_{GNSS} + 3$(m)
$\delta V_{GNSS} = \delta V_{GNSS} + 1$(m/s)
$\delta P_{GNSS} = \delta P_{GNSS} + 6$(m)
$\delta V_{GNSS} = \delta V_{GNSS} + 2$(m/s)</td></tr>
</table>

7	700 s < t < 800 s 1700 s < t < 1800 s 2700 s < t < 2800 s	$\varepsilon_k = \varepsilon_k + (0.036\ ^\circ/\mathrm{h})*t$	Soft faults
		$\varepsilon_k = \varepsilon_k + (0.36\ ^\circ/\mathrm{h})*t$	
8	800 s < t < 900s 1800 s < t < 1900 s 2800 s < t < 2900 s	$\varepsilon_k = \varepsilon_k + (0.18\ ^\circ/\mathrm{h})*t$	
		$\varepsilon_k = \varepsilon_k + (1.8\ ^\circ/\mathrm{h})*t$	

Figure 6 shows the detection results for the minor faults in Table 2 when the detection threshold and sliding window width were disregarded. Figure 6(a) shows that neither GNSS nor SINS faults were detected by the LSTM-based fault detection subnetwork. This demonstrates that a neural network alone is not ideal for detecting the original residual time-domain signal of an integrated navigation system and that the fault detection capability seems weak. Figure 6(b) shows that the multi-feature time-domain fault detection subnetwork did not detect some faults when the fluctuation of J_N was unclear. Some SINS soft faults were detected in the steady state but were not obvious during the turning phase. This is because ship maneuvers are conducive to the convergence of state errors in the integrated navigation system, which results in small residuals and unclear covariance characteristics. Figure 6(c) shows the features extracted by STFT, and Fig. 6(d) shows the results of the frequency-domain fault detection subnetwork. Although additional faults, including SINS soft faults, were detected, there were several false alarms, particularly during large changes in course. As shown in Fig. 6(e), the decision-level fusion network combined the advantages of the time-domain statistical characteristics with frequency-domain networks, which not only increased the fault detection accuracy but also decreased the false alarm rate.

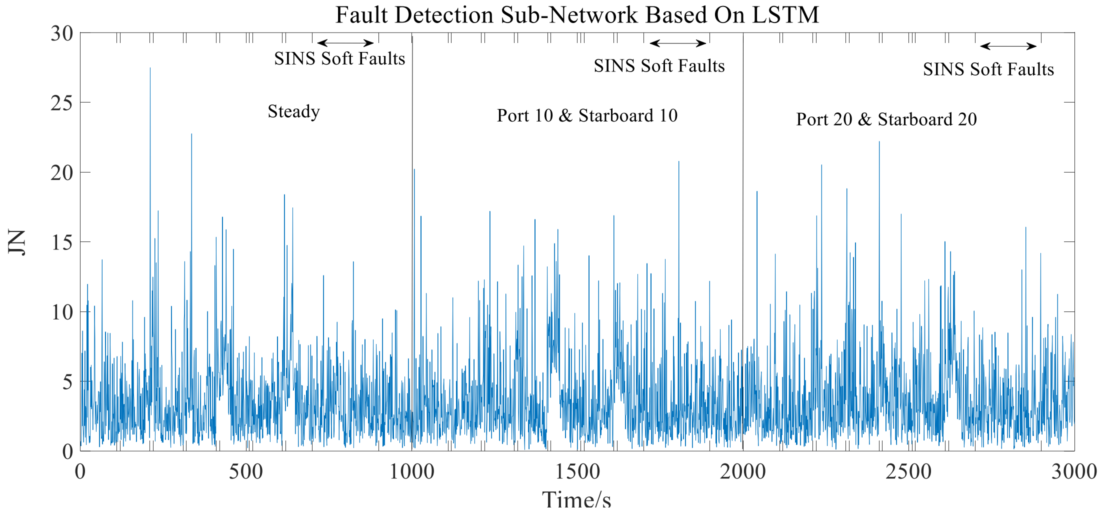

(a) LSTM-based fault detection subnetwork.

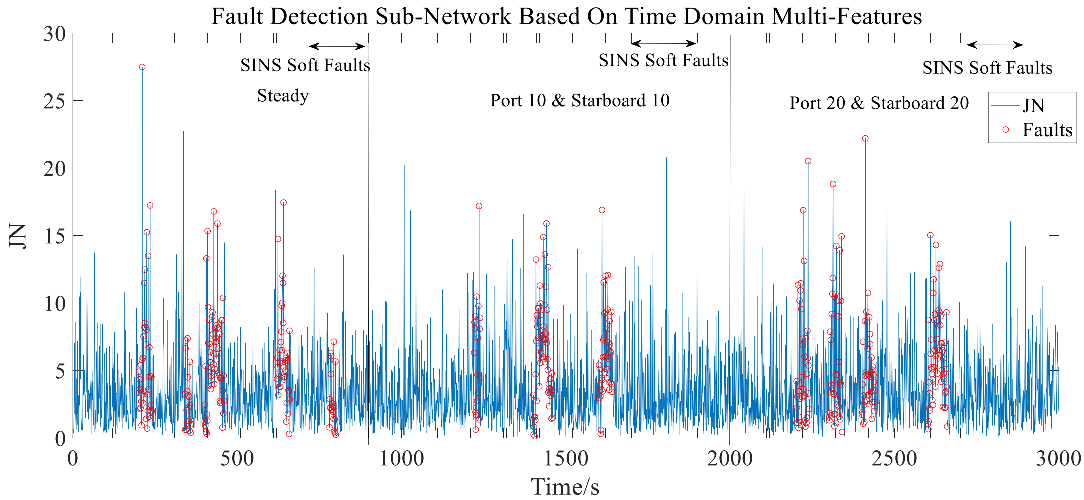

(b) Multi feature time-domain fault detection subnetwork.

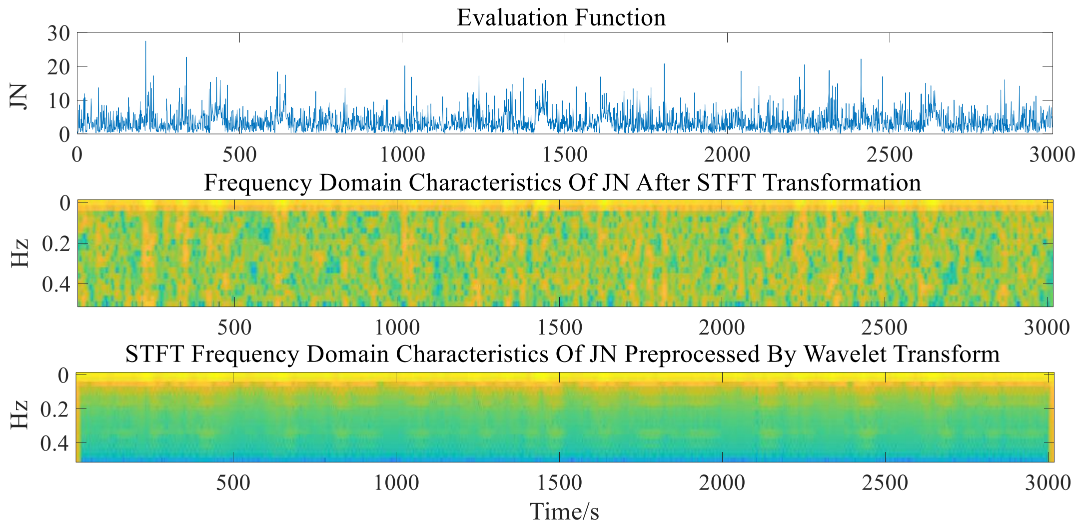

(c) STFT extraction of residual frequency-domain features.

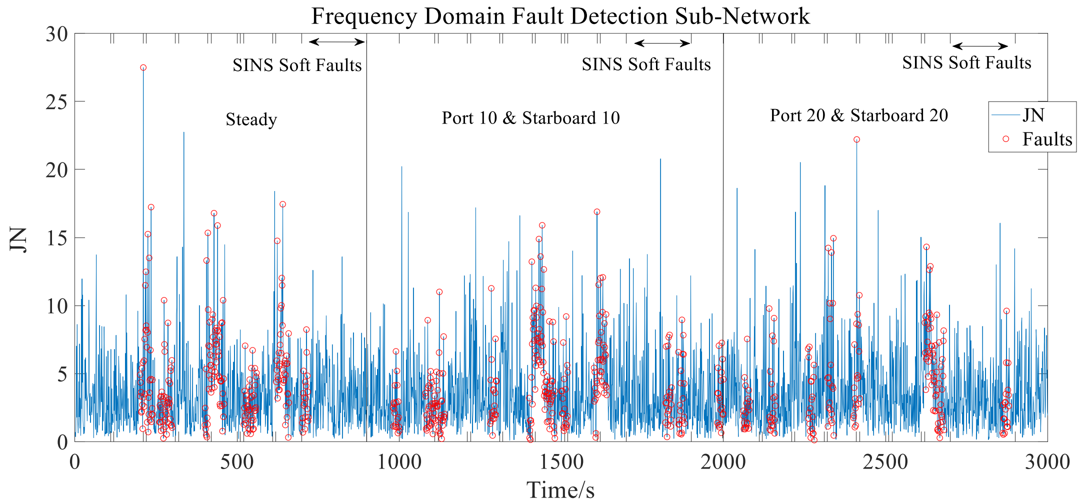

(d) Frequency-domain fault detection subnetwork.

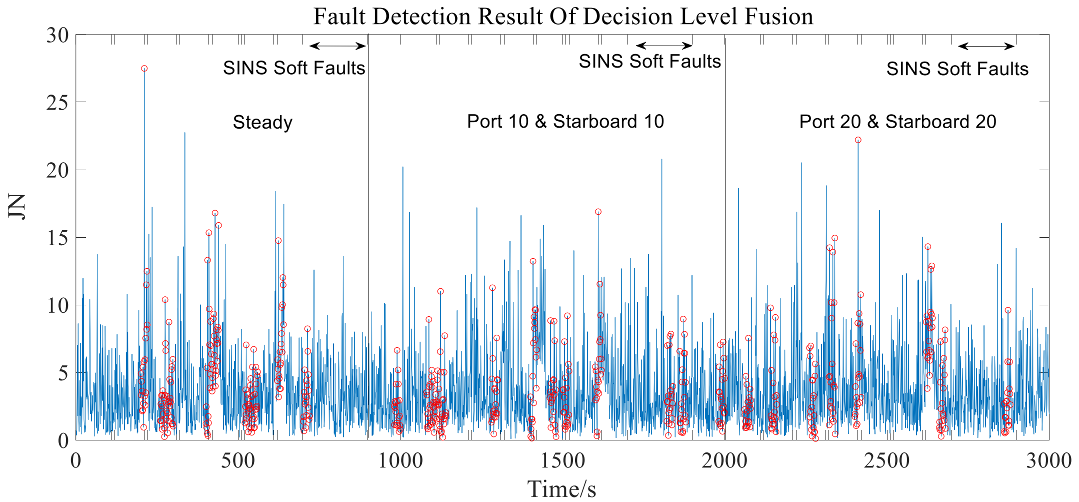

(e) Decision-level fusion network.

Figure 6. Minor fault detection results of the proposed algorithm with neural network optimization.

Figure 7 shows the detection results for the major fault cases in Table 2. In contrast to the results for the minor fault cases, Fig. 7(a) shows that the LSTM-based fault detection subnetwork detected a small number of GNSS velocity and position faults. However, the effectiveness was not ideal. Figure 7(b) shows that the multi-feature time-domain fault detection subnetwork detected additional faults during the course alteration stage, but there were some false alarms. Figure 7(c) shows the STFT extraction of the frequency-domain signal J_N, and Fig. 7(d) shows the results of the frequency-domain fault detection subnetwork. There were fewer false alarms and a higher degree of accuracy when compared to the multi feature time-domain fault detection subnetwork. Figure 7(e) shows the results of the decision-level fusion network, which were similar to the results shown in Fig. 7(d).

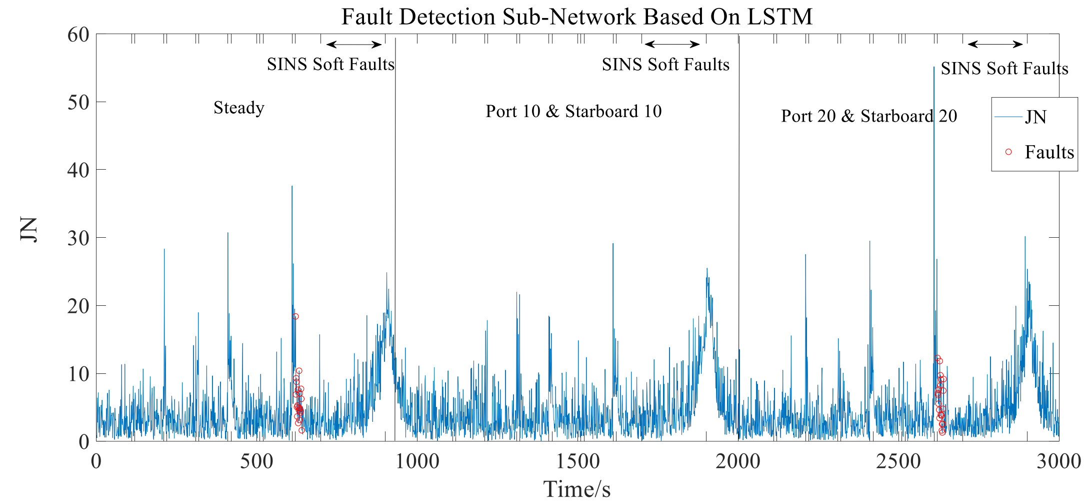

(a) LSTM-based fault detection subnetwork.

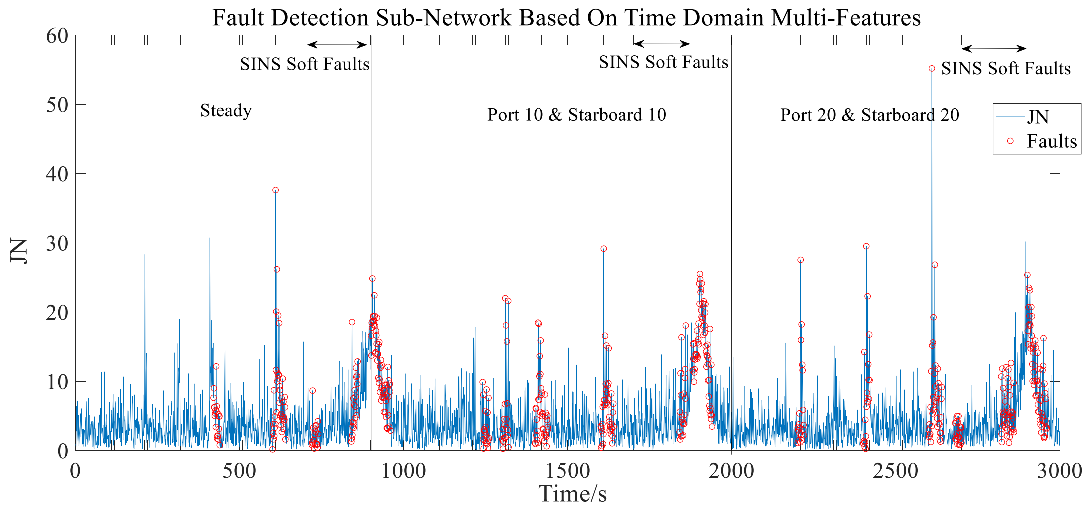

(b) Multi feature time-domain fault detection subnetwork.

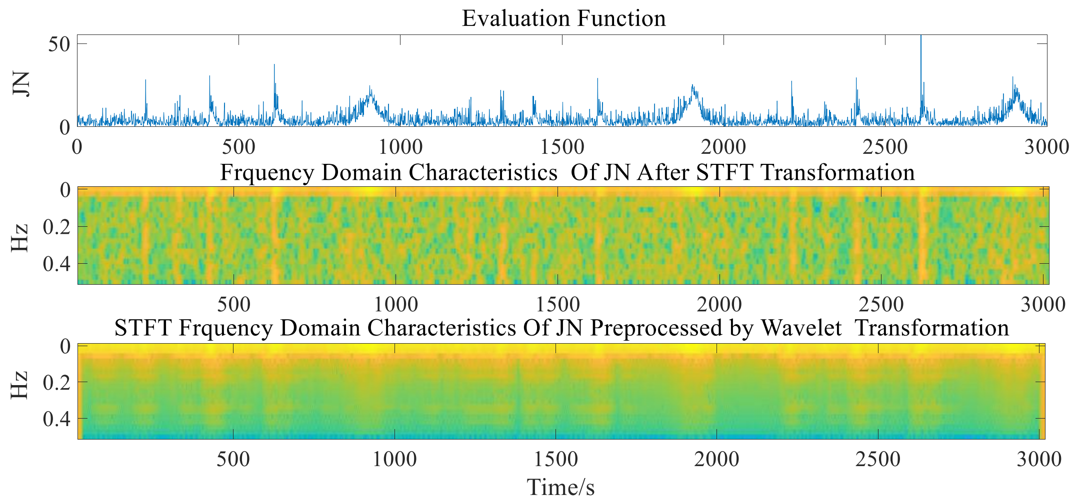

(c) STFT extraction of residual frequency-domain features.

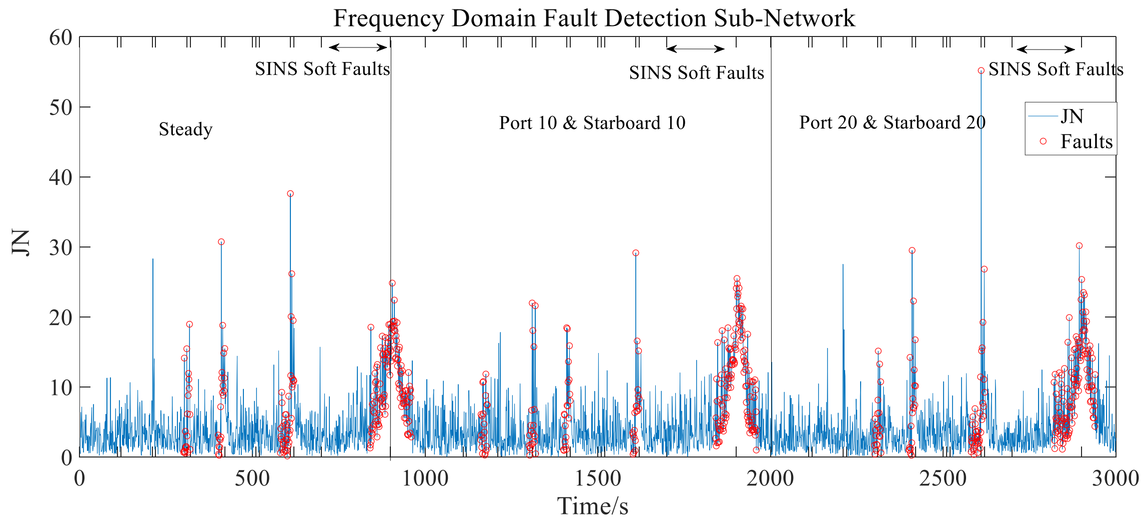

(d) Frequency-domain fault detection subnetwork.

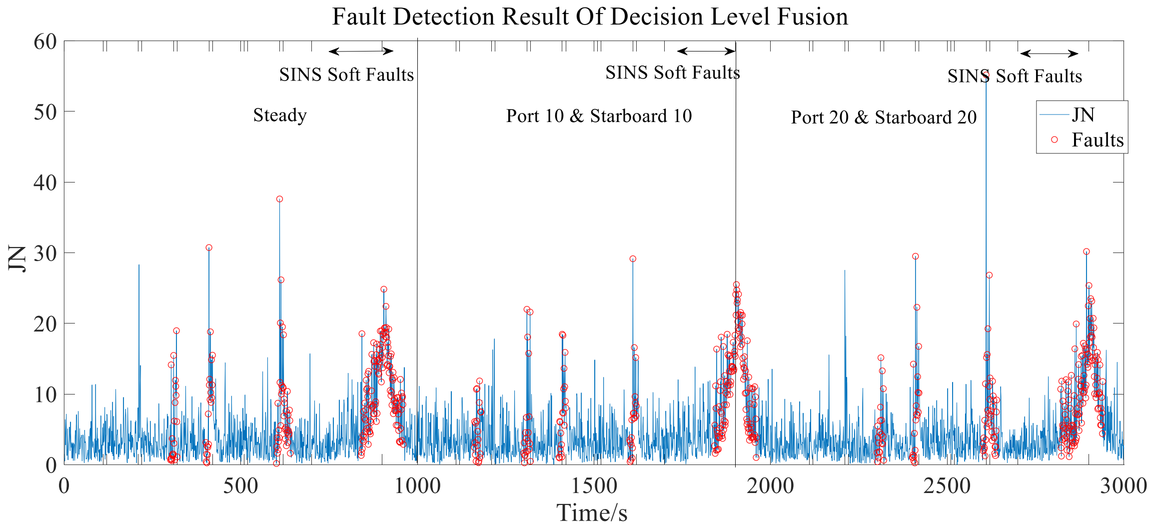

(e) Decision-level fusion network.

Figure 7. Major fault detection results of the proposed algorithm with neural network optimization.

In summary, the proposed fault detection algorithm optimized using a cascaded neural network was capable of detecting faults regardless of the various motion states of the ASS without replying on an empirical threshold and designed sliding window width. The LSTM-based fault detection subnetwork had a low degree of generality, a low detection rate, and a negligible effect on the results of the decision-level fusion network. The multi-feature time-domain fault detection subnetwork missed minor faults but had a minimal false alarm rate. The frequency-domain fault detection subnetwork detected most faults, including SINS soft faults, but had a high false alarm rate. The decision-level fusion network combined the advantages of the three subnetworks by detecting most faults, including soft faults, but also realizing a low false alarm rate. Thus, the optimization of the proposed algorithm was verified. It is worth noting that it is difficult to determine which period the failure occurred based on the values of the vertical axis of the blue residual lines based on the traditional residual observer-based fault detection algorithms. According to previous studies (Fei et al. 2021, Liang et al, 2021, Oh et al. 2022, Zammali et al. 2021) limited by the algorithm principle, the fault detection algorithms based on residual observer are generally insensitive to gradual soft faults. Simply optimizing the residual parameters cannot make it sensitive to soft faults. In this paper, due to a lack of a large number of real ship data, the cascaded network is used to optimize it, and the result of soft fault detection is better than the traditional algorithm.

4.2 Experimental result and discussion

To confirm the effectiveness of the proposed algorithm in practical applications, real historical ship data were applied to the simulation-trained model. Faults were introduced into the historical sensor data to determine whether they could be detected using the proposed algorithm with various integrated navigation systems. The historical data were obtained from an experiment conducted using ASS 320 at Lingshui Port in Dalian, China. The experimental historical track included straight lines and turns. The experimental site is 170 m in length and 70 m in width. The bay is not considerably affected by tidal waves, and the current is slow. An Mti-G-710, a Lidar, cameras, a 4G communication antenna, and a 5.8G WIFI antenna were installed on top of ASS 320. Moreover, ASS 320 was equipped with COMPASS and DVL, as shown in Fig. 8. To accurately simulate interference during actual navigation, the speed measured using DVL was subjected to sinusoidal function interference with an amplitude of 0.5 m/s. The experimental data covered a period of 437 s. Then, 0.18°/h SINS soft faults were added at 101–150 s, and 1 m/s of GNSS velocity faults and 1 m/s of DVL faults were added at 201–230 s and 301–330 s, respectively. The proposed algorithm was then applied to fault detection for verification.

Figure 8. Field test of ASS 320 and the experimental route.

Figure 9 shows that the results of the SINS/GNSS integrated navigation system were comparable to the simulation results. Figure 9(a) shows that the LSTM-based fault detection subnetwork continued to perform poorly in terms of fault detection. Figure 9(b) shows that the multi-feature time-domain fault detection subnetwork detected most SINS soft faults between 100 and 150 s but had some false alarms after 250 s. Figure 9(c) shows the STFT extraction results, and Fig. 9(d) shows that the frequency-domain fault detection subnetwork had a large number of false alarms between 150 and 200 s. Figure 9(e) shows that the decision-level fusion network not only achieved a lower false alarm rate than the frequency-domain fault detection subnetwork did but also successfully detected most faults, including SINS soft faults.

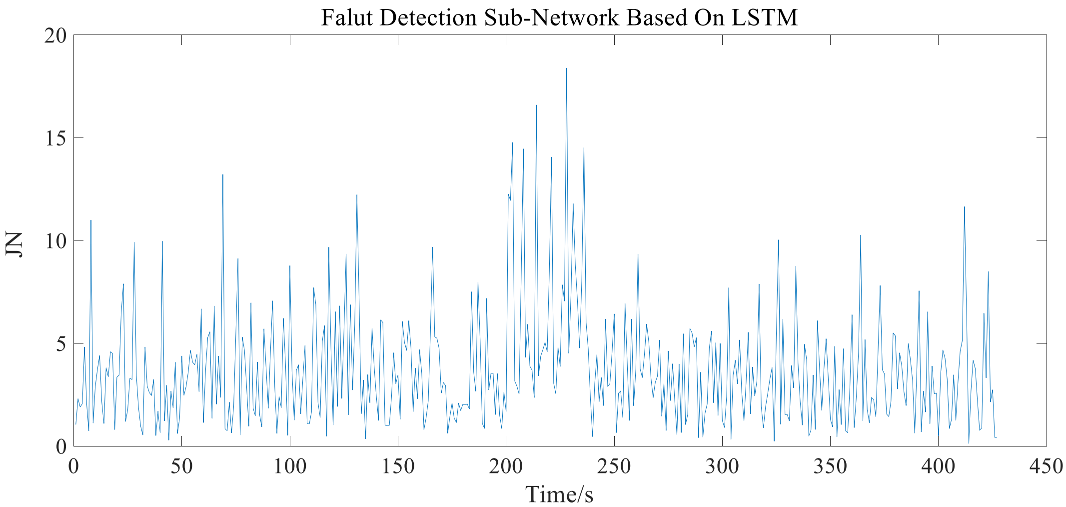

(a) LSTM-based fault detection subnetwork.

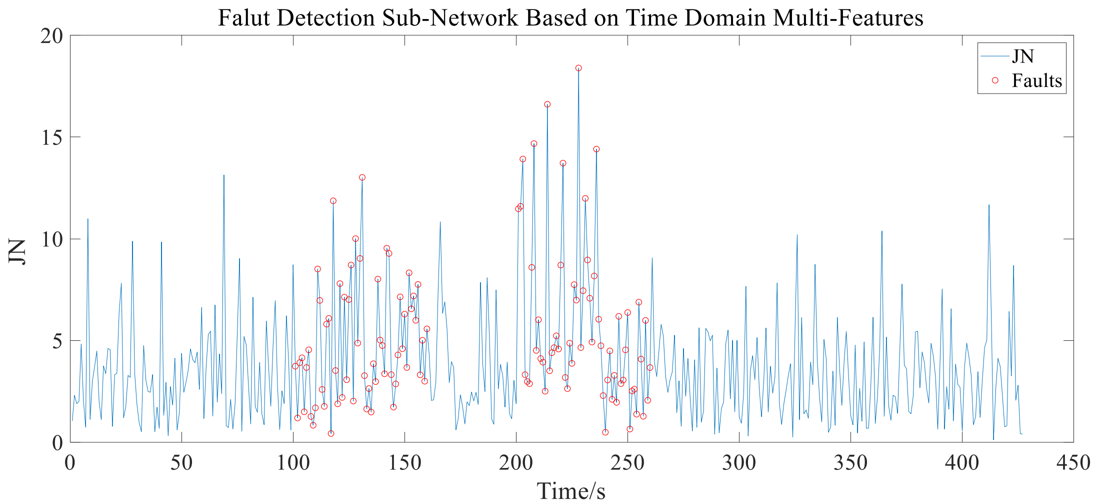

(b) Multi feature time-domain fault detection subnetwork.

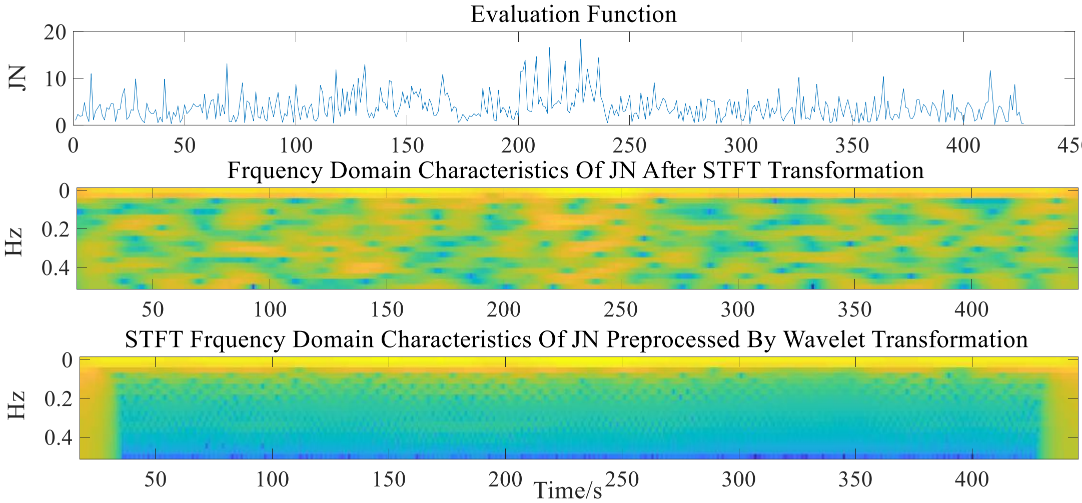

(c) STFT extraction of residual frequency-domain features.

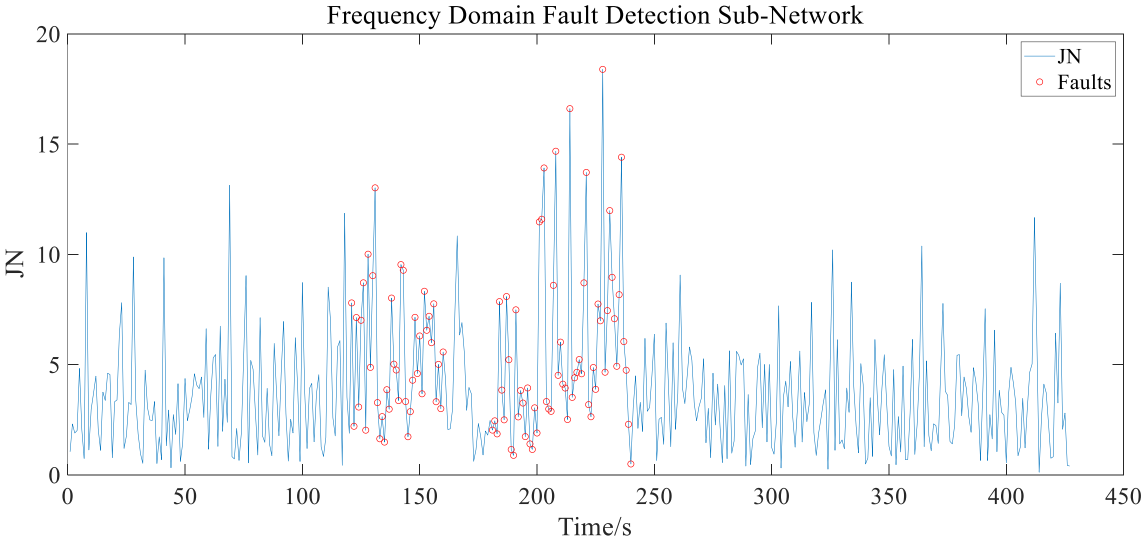

(d) Frequency-domain fault detection subnetwork.

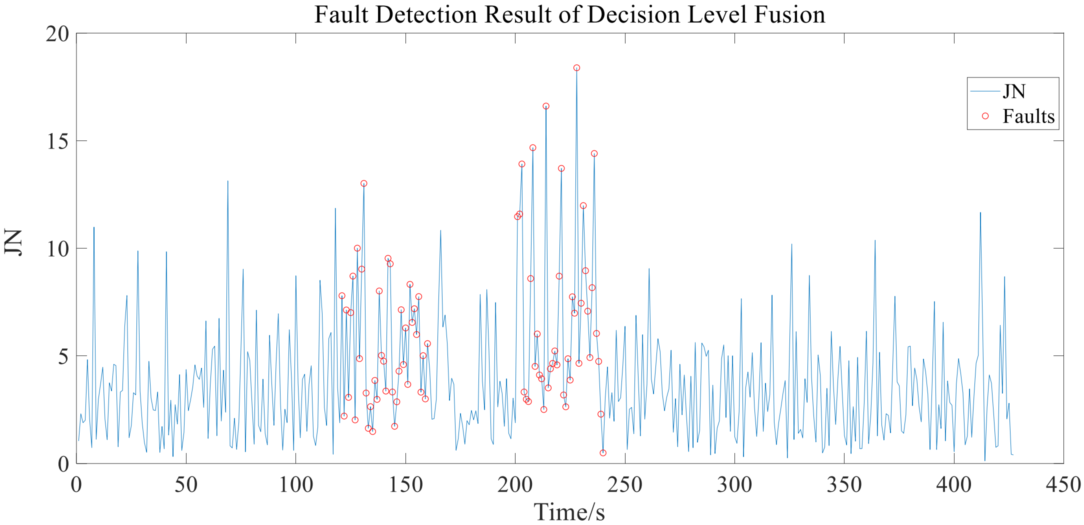

(e) Decision-level fusion network.

Figure 9. Fault detection results of the proposed algorithm with neural network optimization for the SINS/GNSS integrated navigation system of ASS 320.

The proposed algorithm was adopted for the SINS/DVL/COMPASS integrated navigation system. Figure 10 shows that similar results were obtained as in the previous cases. Figure 10(b) shows that the multi-feature time-domain fault detection subnetwork had a higher number of false alarms. Figures 10(d) and (e) show that the decision-level fusion network and frequency-domain fault detection subnetwork had similar results and successfully detected SINS soft faults without obvious fluctuations in J_N and with a low number of false alarms.

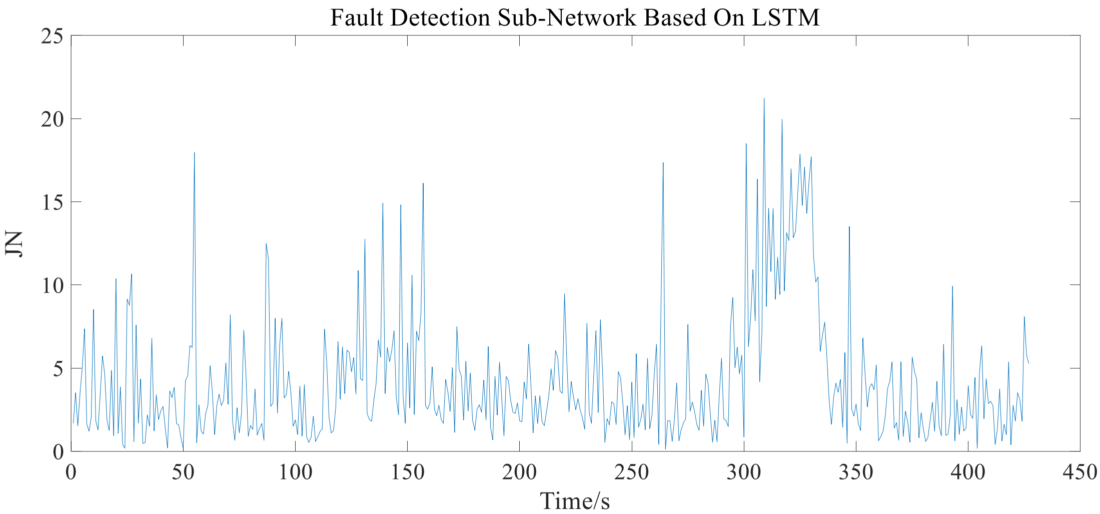

(a) LSTM-based fault detection subnetwork.

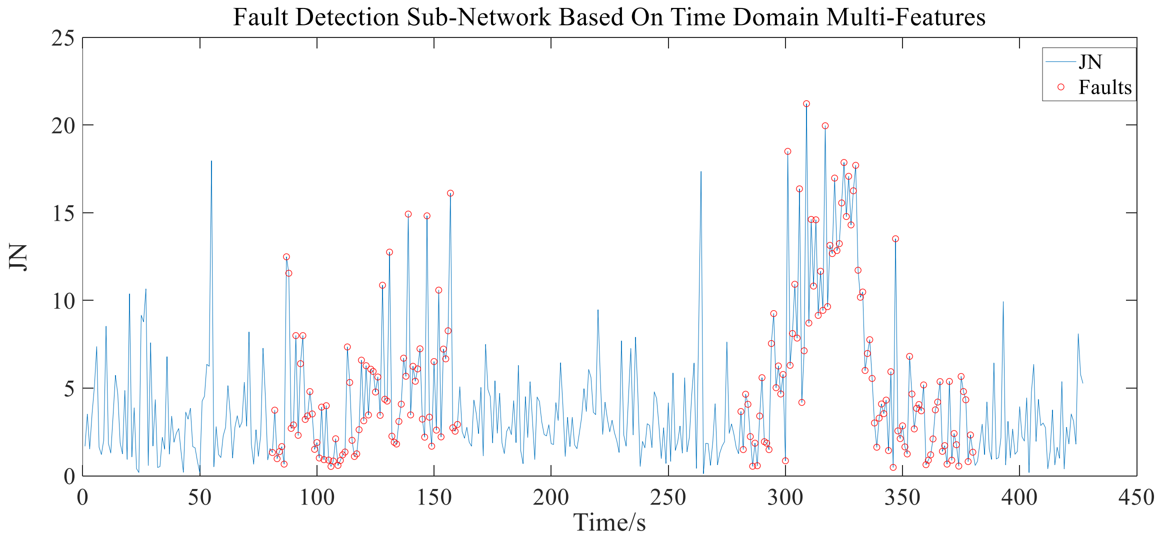

(b) Multi feature time-domain fault detection subnetwork.

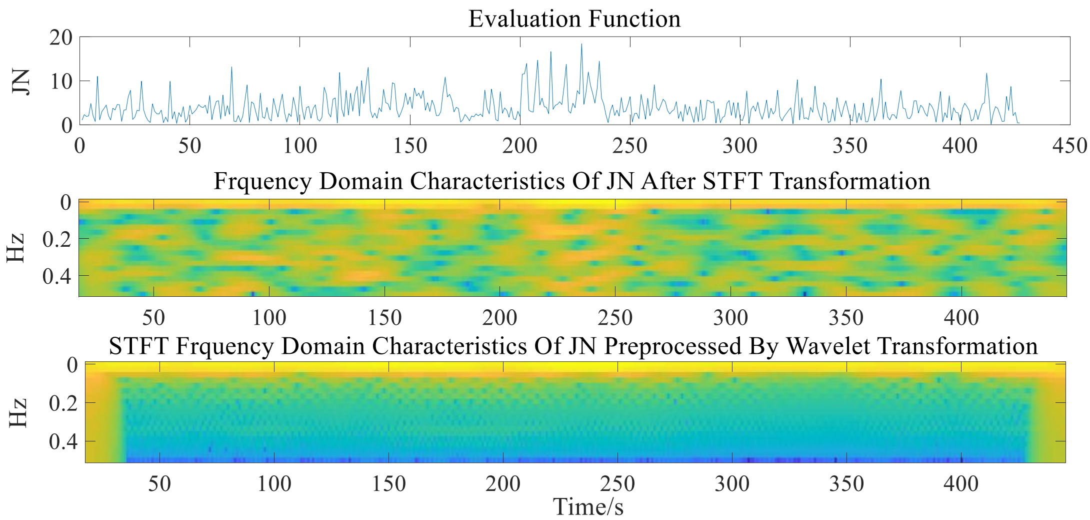

(c) STFT extraction of residual frequency-domain features.

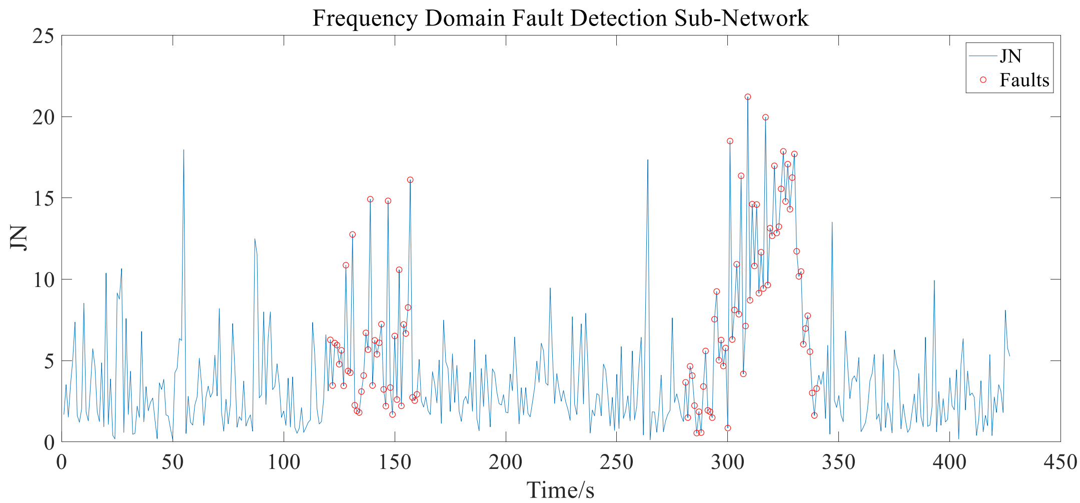

(d) Frequency-domain fault detection subnetwork.

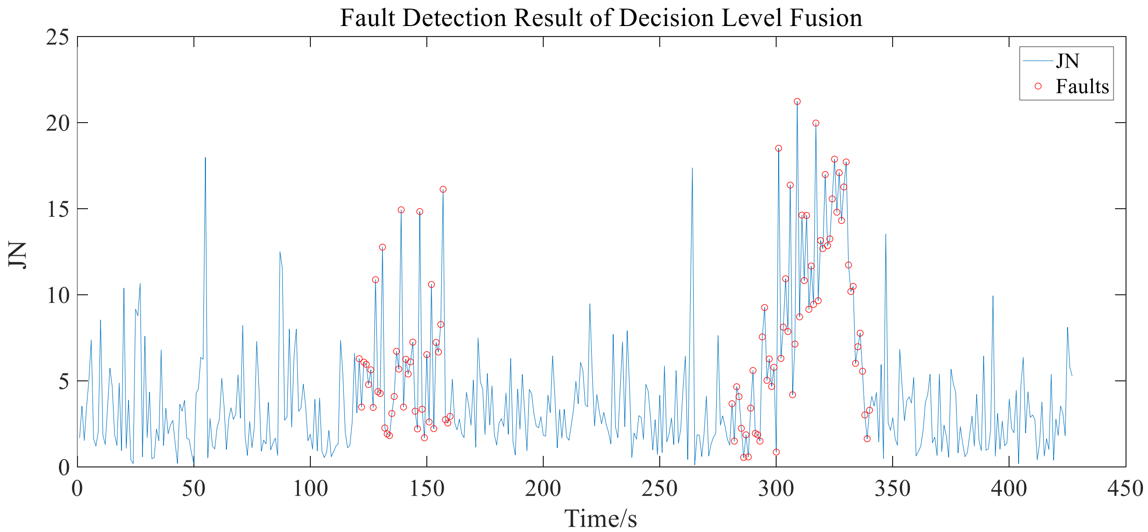

(e) Decision-level fusion network.

Figure 10. Fault detection results of the proposed algorithm with neural network optimization for the SINS/DVL/COMPASS integrated navigation system of ASS 320.

The experimental results verified that the proposed algorithm could detect faults in the integrated navigation system of an ASS. The proposed algorithm was capable of detecting slowly changing SINS soft faults while retaining a low false alarm rate for SINS/GNSS and SINS/DVL/COMPASS integrated navigation systems. The LSTM-based fault detection subnetwork was not sensitive to such faults, but the frequency-domain fault detection subnetwork and multi feature time-domain fault detection subnetwork had significant impacts on the overall results. The multi feature time-domain fault detection subnetwork had a high false alarm rate for both integrated navigation systems.

5. Conclusion

Previous studies on the fault detection of integrated navigation systems for ASSs have shown that setting the fault detection threshold is highly dependent on experience, the sliding window width is difficult to design, SINS gradient soft faults are difficult to detect, and previous algorithms cannot be learned online. In this study, a fault detection algorithm was proposed to address the above issues. The proposed algorithm was optimized using a cascaded neural network comprising an LSTM-based fault detection subnetwork, multi feature time-domain fault detection subnetwork, and frequency-domain fault detection subnetwork. The algorithm uses residual and covariance information during the filtering process to eliminate the dependence of traditional model-based fault detection algorithms on empirical parameter settings. This solved the problem of the residual observer being insensitive to soft faults. The proposed algorithm was verified through simulations and historical data from a real ship. The LSTM-based fault detection subnetwork had limited effectiveness at detection of time-domain soft faults. Although the multi feature time-domain fault detection subnetwork was capable of detecting SINS soft faults, it had a high rate of missed detection. In contrast, the frequency-domain fault detection subnetwork had a high detection rate but also had a large number of false alarms. The results of the three subnetworks were output to the decision-level fusion network to obtain the optimal results. The results showed that the proposed algorithm is capable of not only detecting soft faults without relying on an empirical threshold but also reducing the rate of missed detections and false alarm for two integrated navigation systems (i.e., SINS/GNSS and SINS/DVL/COMPASS). The detection performance with the decision-level fusion network was better than that of a single subnetwork. This confirmed the effectiveness of the proposed algorithm and neural network optimization.

Appendix I CKF algorithm for an integrated navigation system

For the time update, the mean and variance of the posterior probability of the system under the measurement conditions are approximated by transforming $2n$ cubature points with equal weights $\frac{1}{2n}$ using the nonlinear system equation $f_c(.)$. The propagated i-th sampling points cubature points at step k can be computed as

$$\begin{aligned} &\chi_{k-1}^{(i)} = \sqrt{nP_{k-1}} + \hat{x}_{k-1} \quad (i = 1, 2, ..., 2n) \\ &\overline{\chi}_{k-1}^{(i)} = f_c(\chi_{k-1}^{(i)}) \end{aligned} \tag{25}$$

The one-step state prediction $\hat{x}_{k|k-1}$ and prediction variance $P_{xx,k|k-1}$ are computed as

$$\begin{aligned} &\hat{x}_{k|k-1} = \frac{1}{2n}\sum_{i=1}^{2n}\overline{\chi}_{k-1}^{(i)} \\ &P_{xx,k|k-1} = \frac{1}{2n}\sum_{i=1}^{2n}\overline{\chi}_{k|k-1}^{(i)}(\overline{\chi}_{k|k-1}^{(i)})^{\mathrm{T}} - (\hat{x}_{k|k-1})(\hat{x}_{k|k-1})^{\mathrm{T}} + Q_{k+1} \end{aligned} \tag{26}$$

For the measurement update, the volume point is calculated according to the estimation $\hat{x}_{k|k-1}$ and variance $P_{xx,k|k-1}$ at time k. Q_k denotes the system noise covariance.

$$\begin{aligned} &\xi_{k|k-1}^{(i)} = \sqrt{nP_{k|k-1}} + \hat{x}_{k|k-1} \quad (i = 1, 2, ..., 2n) \\ &\overline{z}_{k|k-1}^{(i)} = H_t(\xi_{k|k-1}^{(i)}) \end{aligned} \tag{27}$$

The measurement prediction $\hat{z}_{k|k-1}$, measurement prediction error variance (innovation variance) $P_{zz,k|k-1}$, and state measurement cross covariance $P_{xz.k|k-1}$ can be obtained as follows:

$$\begin{aligned} &\hat{z}_{k|k-1} = \frac{1}{2n}\sum_{i=1}^{2n}\overline{z}_{k|k-1}^{(i)} \\ &P_{zz,k|k-1} = \frac{1}{2n}\sum_{i=1}^{2n}\overline{z}_{k|k-1}^{(i)}(\overline{z}_{k|k-1}^{(i)})^{\mathrm{T}} - \hat{z}_{k|k-1}(\hat{z}_{k|k-1})^{\mathrm{T}} + R_k \\ &P_{xz.k|k-1} = \frac{1}{2n}\sum_{i=1}^{2n}\xi_{k|k-1}^{(i)}(\overline{z}_{k|k-1}^{(i)})^{\mathrm{T}} - \hat{x}_{k|k-1}(\hat{z}_{k|k-1})^{\mathrm{T}} \end{aligned} \tag{28}$$

The measurement update of the gain K_k, state prediction vector $\hat{x}_{k|k}$, and state prediction covariance matrix $P_{k|k}$ can be performed as follows:

$$\begin{aligned} &K_k = P_{xz,k|k-1} / P_{zz,k|k-1} \\ &\hat{x}_{k|k} = \hat{x}_{k|k-1} + K_k(z_k - \hat{z}_{k|k-1}) \\ &P_{k|k} = P_{k|k-1} - K_k P_{zz,k|k-1} K_k^{\mathrm{T}} \end{aligned} \tag{29}$$

Appendix II List of notation

Most of the symbols are introduced in detail in the main text. Some symbols with subscripts are further explained below.

L_t^{SINS} : Latitude measured by SINS at time t.

λ_t^{SINS} : Longitude measured by SINS at time t.

h_t^{SINS} : Height measured by SINS at time t.

L_t^{GNSS} : Latitude measured by GNSS at time t.

λ_t^{GNSS} : Longitude measured by GNSS at time t.

h_t^{GNSS} : Height measured by GNSS at time t.

$V_{E,t}^{SINS}$: Eastern velocity measured by SINS at time t.

$V_{N,t}^{SINS}$: Northern velocity measured by SINS at time t.

$V_{H,t}^{SINS}$: Vertical velocity measured by SINS at time t.

$V_{E,t}^{GNSS}$: Eastern velocity measured by GNSS at time t.

$V_{N,t}^{GNSS}$: Northern velocity measured by GNSS at time t.

$V_{H,t}^{GNSS}$: Vertical velocity measured by GNSS at time t.

$V_{E,t}^{DVL}$: Eastern velocity measured by DVL at time t.

$V_{N,t}^{DVL}$: Northern velocity measured by DVL at time t.

ψ_t^{SINS} : Heading measured by SINS at time t.

$\psi_t^{COMPASS}$: Heading measured by compass at time t.

B_c : System noise transfer matrix.

$B_{cf,t}$: SINS fault transition matrix.

$D_{cf,t}$: Measurement fault transition matrix.

$\tilde{S}(.)$: Function of the covariance inner product after whitening.

Disclosure statement

No potential conflict of interest was reported by the authors.

Funding

This work was supported by the National Nature Science Foundation of China [grant numbers 51579024, 51879027, 61374114] and Applied Basic Research Plan of Liaoning Province in 2022 (2022JH2/101300265). This work is partially supported by Royal Society research grant (RGS/R2/212343)

References

Chen, J., & Patton, J. R. (2000). Standard H∞ filtering formulation of robust fault detection. *IFAC Proceedings Volumes*, *33*(11), 261-266.

Chen, J., Zhang, S., Cao, Y., Li, H., & Zheng, H. (2020). A robust fault detection algorithm for the GNSS/INS integrated navigation systems. *Journal of Geodesy and Geoinformation Science*, *3*(1), 12-24.

Du, B., Ru, L., Wu, C., & Zhang, L. (2019). Unsupervised deep slow feature analysis for change detection in multi-temporal remote sensing images. *IEEE Transactions on Geoscience and Remote Sensing*, *57*(12), 9976-9992.

Fan, C., Wróbel, K., Montewka, J., Gil, M., Wan, C., & Zhang, D. (2020). A framework to identify factors influencing navigational risk for Maritime Autonomous Surface Ships. *Ocean Engineering*, *202*, 107188.

Fei, Z., Wang, X., & Wang, Z. (2021).Event-based fault detection for unmanned surface vehicles subject to denial-of-service attacks[J]. *IEEE Transactions on Systems, Man, and Cybernetics: Systems*, *52*(5), 3326-3336.

Gao, Z., Cecati, C., & Ding, S. X. (2015). A survey of fault diagnosis and fault-tolerant techniques—Part I: Fault diagnosis with model-based and signal-based approaches. *IEEE Transactions on Industrial Electronics*, *62*(6), 3757-3767.

Gao, Z., Cecati, C., & Ding, S. X. (2015). A survey of fault diagnosis and fault-tolerant techniques—Part II: Fault diagnosis with knowledge-based and hybrid/active approaches. *IEEE Transactions on Industrial Electronics*, *62*(6), 3768-3774.

Guo, D., Zhong, M., Ji, H., Liu, Y., & Yang, R. (2018). A hybrid feature model and deep learning based fault diagnosis for unmanned aerial vehicle sensors. *Neurocomputing*, *319*, 155-163.

Jin, H. S., Cho, H., Jiafeng, H., Lee, J. H., Kim, M. J., Jeong, S. K.,... & Choi, H. S. (2022). Hovering control of UUV through underwater object detection based on deep learning. *Ocean Engineering*, *253*, 111321.

Khan, A. Q., Abid, M., & Ding, S. X. (2014). Fault detection filter design for discrete-time nonlinear systems-A mixed H-_H∞ optimization. *Systems & Control Letters*, *67*, 46-54.

Li, B., Chen, W., Peng, Y., Dong, D., Wang, Z., Xiao, T.,... & Liu, M. (2020). Robust Kalman filtering based on chi-square increment and its application. *Remote Sensing*, *4*(12), 732.

Li, X., Yang, Y., Hu, N., Cheng, Z., & Cheng, J. (2021). Discriminative manifold random vector functional link neural network for rolling bearing fault diagnosis. *Knowledge-Based Systems*, *211*, 106507.

Liang, D., Yang, Y., Li, R., & Liu, R. (2021). Finite-frequency H_{-}/H_{∞} unknown input observer-based distributed fault detection for multi-agent systems. *Journal of the Franklin Institute*, 2021, *358*(6), 3258-3275.

Liu, H., Zhong, M., & Liu, Y. (2018). Fault diagnosis for a kind of nonlinear systems by using model-based contribution analysis. *Journal of the Franklin Institute*, *355*(16), 8158-8176.

Liu, H., Zhong, M., & Liu, Y. (2019). A new residual evaluation function based fault diagnosis for a kind of nonlinear systems. *Asian Journal of Control*, *21*(3), 1153-1165.

Liu, Z., Zhang, Y., Yu, X., & Yuan, C. (2016). Unmanned surface vehicles An overview of developments and challenges. *Annual Reviews in Control*, *41*, 71-93.

Miao, L., & Shi, J. (2014). Model-based robust estimation and fault detection for MEMS-INS/GPS integrated navigation systems. *Chinese Journal of Aeronautics*, *27*(4), 947-954.

Oh, Y., Kim, Y., Na, K., & Youn, B. D. (2022). A deep transferable motion-adaptive fault detection method for industrial robots using a residual–convolutional neural network. I*SA Transactions*, *128*, 521-534.

Shen, K., Wang, M., Fu, M., Yang, Y., & Yin, Z. (2019). Observability analysis and adaptive information fusion for integrated navigation of unmanned ground vehicles. *IEEE Transactions on Industrial Electronics*, *67*(9), 7659-7668.

Sun, R., Wang, J., Cheng, Q., Mao, Y., & Ochieng, W. Y. (2021). A new IMU-aided multiple GNSS fault detection and exclusion algorithm for integrated navigation in urban environments. *GPS Solutions*, *25*(4), 1-17.

Tao, H., Wang, P., Chen, Y., Stojanovic, V., & Yang, H. (2019). An unsupervised fault diagnosis method for rolling bearing using STFT and generative neural networks. *Journal of the Franklin Institute*, *357*(11), 7286-7307.

Thombre, S., Zhao, Z., Ramm-Schmidt, H., García, J. M. V., Malkamäki, T., Nikolskiy, S.,... & Lehtola, V. V. (2022). Sensors and ai techniques for situational awareness in autonomous ships: A review. *IEEE Transactions on Intelligent Transportation Systems*, *23*(1), 64-83.

Wang, Q., & Zhang, M. (2022). Inertial navigation system gyroscopic on-line calibration assisted by marine star sensor based on forgetting factor selection of a Sage-Husa filter. *Journal of Marine Engineering & Technology*, *21*(1), 1-8.

Wang, Q., Cui, X., Li, Y., & Ye, F. (2017). Performance enhancement of a USV INS/CNS/DVL integration navigation system based on an adaptive information sharing factor federated filter. *Sensors*, *17*(2), 239.

Wei, W., Gao, S., Zhong, Y., Gu, C., & Hu, G. (2018). Adaptive square-root unscented particle filtering algorithm for dynamic navigation. *Sensors*, *18*(7), 2337.

Xi, W., Li, Z., Tian, Z., & Duan, Z. (2018). A feature extraction and visualization method for fault detection of marine diesel engines. *Measurement*, *116*, 429-437.

Yang, H., Meng, C., & Wang, C. (2020). A hybrid data-driven fault detection strategy with application to navigation sensors. *Measurement and Control*, *53*(7-8), 1404-1415.

Yu, Z., Zhang, Q., Yu, K., & Zheng, N. (2021). A state-domain robust chi-square test method for GNSS/INS integrated navigation. *Journal of Sensors*, *2021*, 1745383.

Zammali, C., Van Gorp, J., Wang, Z., & Raïssi, T. (2021). Sensor fault detection for switched systems using interval observer with L_∞ performance. *European Journal of Control*, *57*, 147-156.

Zanoli, S. M., Astolfi, G., Bruzzone, G., Bibuli, M., & Caccia, M. (2012). Application of fault detection and isolation techniques on an unmanned surface vehicle (USV). *IFAC Proceedings Volumes*, *45*(27), 287-292.

Zhang, H., Li, C., Li, D., Zhang, Y., & Peng, W. (2021). Fault detection and diagnosis of the air handling unit via an enhanced kernel slow feature analysis approach considering the time-wise and batch-wise dynamics. *Energy and Buildings*, *253*, 111467.

Zhong, L., Liu, J., Li, R., & Wang, R. (2017). Approach for detecting soft faults in GPS/INS integrated navigation based on LS-SVM and AIM. *The Journal of Navigation*, *70*(3), 561-579.

Zhong, M., Ding, S. X., & Ding, E. L. (2010). Optimal fault detection for linear discrete time-varying systems. *Automatica*, *46*(8), 1395-1400.

Zhong, M., Guo, J., Guo, D., & Yang, Z. (2016). An extended Hi/H∞ optimization approach to fault detection of INS/GPS-integrated system. *IEEE Transactions on Instrumentation and Measurement*, *65*(11), 2495-2504.

Zhong, M., Liu, H., & Song, N. (2015). On designing an extended Hi/H∞-FDF for a class of nonlinear Systems. *IFAC-PapersOnLine*, *48*(12), 707-712.

Zhu, Y., Cheng, X., & Wang, L. (2016). A novel fault detection method for an integrated navigation system using Gaussian process regression. *The Journal of Navigation*, *69*(4), 905-919.

Zhuang, Z., Lv, H., Xu, J., Huang, Z., & Qin, W. (2019). A deep learning method for bearing fault diagnosis through stacked residual dilated convolutions. *Applied Sciences-Basel*, *9*(9), 1823-1841.